EM STUDY OF CRYSTALLOGRAPHY AND PHASE RELATIONSHIPS IN THE Be_3N_2-$BeSiN_2$ SYSTEM

Contents

EM STUDY OF CRYSTALLOGRAPHY AND PHASE RELATIONSHIPS IN THE Be_3N_2-$BeSiN_2$ SYSTEM

Thomas McCarroll Shaw

Materials and Molecular Research Division
and
Materials Science and Engineering
Lawrence Berkeley Laboratory
University of California
Berkeley, California 94720

ABSTRACT

Transmission electron microscopy and diffraction have been used to examine structural aspects of phases along the $BeSiN_2$-Be_3N_2 tie line of the Be-Si-O-N system.

Electron diffraction experiments are found to substantiate previous x-ray evidence for the derived structures of $BeSiN_2$, β Be_3N_2, α Be_3N_2 and the presence of a number of long period superstructures at intermediate compositions.

Real space observations using direct fringe and structure imaging techniques have been made and are in agreement with the 15R polytype structure derived from x-ray diffraction data. In addition, these observations indicate that beryllium atoms are preferentially sited in cubic stacked layers, allowing the polytype structures to be described as a coherent intergrowth of layers of the $BeSiN_2$ and β Be_3N_2 structure.

Further observations made on a non stoichiometric $BeSiN_2$ sample suggests that alternatively the polytypes may be described in terms of a regularly faulted $BeSiN_2$ structure. Each fault changes the coordination of tetrahedral sites from base sharing to edge sharing in the fault, allowing excess beryllium atoms to be accommodated in the close packed nitrogen lattice. For larger deviations from the

Li-Si-Al-O-N systems. Structural determinations using x-ray powder diffraction techniques have identified these phases as being wurtzite polytypes[4,5] in which the unit cell dimensions are determined by composition rather than by the periodicity of displacement faulting. In the Be-Si-O-N system for metal to non-metal atom ratios of $M_{m+1}:X_m$ a series of seven polytypes has been reported at Be_3N_2 rich compositions. The series is bounded by extreme members Be_3N_2, $BeSiN_2$ and BeO (Fig. 1). The index m assumes a minimum value of 2 for β Be_3N_2 and a maximum value of $m = \infty$ corresponding to both the wurtzite structure BeO and the ordered wurtzite structure $BeSiN_2$. The composition dependence of the series can be explained by regular insertion of a cubic stacked layer in which all tetrahedral sites are occupied by metal atoms (composition M_2X) into a hexagonal wurtzite layer arrangement. In the wurtzite structure tetrahedral sites share bases thus only upward or downward pointing sites may be occupied, to give a composition MX. The period of the M_2X layers then determines the overall composition and the unit cell dimensions of each polytype. Non-metal atom stacking in β Be_3N_2 is indicated as

$$A_m^m B_m^m C_m^m B_m A_m^m B_m^m C$$

with alternate M_2X and MX layers. β Be_3N_2 is thus designated as a 4H structure after the notation of Ramsdell.[14] Similarly in the 15R Be_9SiN_{10} ($M_6:X_5$) structure an M_2X layer occurs every fifth layer to produce a unit cell consisting of three rhombohedrally related blocks each containing five close packed layers. In the same way other members

of the series can be produced i.e., 9R, 8H, 12H, 21R and 27R. X-ray analysis of hot pressed samples of these structures has been carried out.[5] Although the agreement of x-ray data with this structure was good, it was felt that electron diffraction and microscopy would provide useful data on local crystallography and structural features of the polytypes not resolvable by x-ray techniques.

The object of this investigation was to examine in detail the crystallography of polytypes in the series Be_3N_2-$BeSiN_2$ using transmission electron microscopy and diffraction techniques. Phase contrast was used to examine stacking periodicities of the close-packed planes and so to characterize disorders occurring in the stacking sequences. Defects in the polytype structures were also examined using contrast experiments and their role in polytype formation examined. Alternative descriptions of the polytype phases in terms of polysynthetic twinning and crystallographic shear were investigated. Where possible the results have been extended to the description of similar series in the Be_3N_2-BeO and other systems.

II. EXPERIMENTAL PROCEDURES

II.1. Materials Preparation

The materials for this study were prepared at the Max Planck institute in Germany. Details of their preparation are given by Huesby[6] and reproduced here. Samples were prepared from Si_3N_4 and reactor grade Be_3N_2 powders. The powders were mixed in CCl_4 with SiO_2 milling balls in an agate planetary ball mill. Mixtures were dried while being continuously stirred until all the CCl_4 evaporated Powder mixes were then hot pressed at 4000 psi for 1 to 2 hr at 1765-1880°C. The temperature was held within the range of +15°C during equilibration. The composition of the samples was analyzed by atomic absorption (for Be) and by gas chromatography for nitrogen content. Phase identification was carried out by x-ray powder analysis using CuK_α (λ = 1.5405Å) radiation. A silicon single crystal was used for calibration.

The following samples were used in this study; the composition and phase constituents are those found by Huesby et al.

(1) Beryllium nitride

composition: β Be_3N_2

structure: β Be_3N_2(4H) (99%)

(2) Beryllium silicon intride

composition: $Be_9Si_3N_{10}$

structure: 15R + trace 8H

(3) Beryllium silicon nitride

composition: $Be_{11}Si_5N_{14}$

structure: 21R + trace 12H

(4) Beryllium silicon nitride

composition: 60% $BeSiN_2$ + 40% $Be_{6.5}Si_{3.5}N_9$

structure: $BeSiN_2$ + 27R

All these specimens have compositions lying along the Be_3N_2-$BeSiN_2$ tie line of the Be-Si-O-N phase diagram (Fig. 1) when represented in equivalents.

Transmission Electron Microscopy

Electron transparent specimens of the above samples were prepared from slabs 10 mm x 5 mm x 3 mm of bulk material as follows. The slabs were mounted, using a low melting point wax, on a cylindrical block of steel which had had the end faces machined parallel. The block was then bolted to the movable arm of a diamond sectioning wheel. A fine diamond wheel lubricated with kerosene, rotating at about 30 rev/min, was used for cutting slices 0.01-0.02 mm thick. The thickness of sections cut was precisely controlled by adjustment of the arm's position using a micrometer screw.

The sections were then mounted on glass slides, again using a low melting point wax, and both sides ground flat using 400 grit paper. the sections were then about 0.01 mm thick. Discs 2.3 mm in diameter were cut from each section using an ultrasonic trepanning tool. Each disc was individually mounted on a glass slide and ground on progressively finer papers (400-600 grit), finishing with polishing on a diamond polishing wheel impregnated with 1μ diamond paste. Each specimen was then turned over and remounted, the other face being finished in the same manner. A thickness of less than 0.004 mm was aimed for at this stage. An effort was made to keep the thickness of the discs

uniform and to prevent excessive rounding of the edges. At all stages of grinding the thickness was carefully monitored using a micrometer. The discs were removed from the slides by dissolving the wax in alcohol. The discs then were mounted of 3 mm copper specimen grids using a small amount of conducting paint.

Specimens thin enough for examination in the electron microscope were prepared by ion beam sputtering using 5 kV argon ions incident on the specimen at an angle of 20°. The final stage of thinning was carried out at an angle of 15° to produce specimens with finely tapered edges. In order to prevent charging of the specimen under the influence of the electron beam and improve image stability in the microscope, a thin (10-30Å thick) layer of carbon was evaporated on one side of the specimen.

Each material was examined by selected area diffraction, conventional imaging and high resolution imaging techniques using the Siemens 102 and Philips 301 microscopes operating at 125 kV and 100 kV respectively. The Siemens 102 was equipped with a high angle tilt stage for precise orientation of the specimen and contrast experiments. High voltage electron microscopy was also employed (Hitachi 650 kV) for examination of thicker areas of the samples and accurate selected area diffraction.

During the examination of specimens in the microscope, extra reflections were observed to appear in the diffraction patterns. The intensity of these reflections increased with longer examination of a single area. After prolonged foil examination, contamination of the specimen surface beams became clearly visible in both dark field and

bright field modes. The extra spots were therefore attributed to the formation of a thin epitaxial layer on the specimen surface under the influence of the electron beam. Analysis of the diffraction patterns containing extra spots and comparison of interplanar specimens with the ASTM index suggested the contamination was beryllium oxide or oxynitride phases. Their rate of formation was greatly reduced by the use of a specimen anti-contamination device.

When high resolution microscopy was employed particular care was taken to use a minimal thickness of evaporated carbon on the specimen so that resolution was not impaired. Some problem was encountered due to a blotchy effect produced by residual carbon at high magnifications. Also all the specimens examined showed evidence of surface etching due to the ion bombardment. These effects, however, did not interfere with interpretation of images in general.

The details of the unit cells used to describe the crystallography of the polytypes are given in Appendix I.

In Appendix II a more detailed description of high resolution fringe and structure imaging techniques used throughout this investigation is given.

III. EXPERIMENTAL RESULTS

III.1. Structure of Be_3N_2

Be_3N_2 has been shown to exist in two forms. α Be_3N_2 has a cubic unit cell a_o = 8.150 with a C rare earth oxide structure. The nitrogen atoms are in a cubic close packed arrangement. The Be atoms occupy tetrahedral sites in an ordered arrangement such that three out or four sites are filled.[15] β Be_3N_2 is a high temperature modification of α Be_3N_2 with a hexagonal unit cell a_o = 2.8413, c_o = 9.693.[16,17] The β Be_3N_2 structure is the equilibrium structure at hot pressing temperatures (1800°C) forming as one end member of the beryllium silicon nitride polytype series. Selected area diffraction patterns from single grains of sample 1 tilted to high symmetry orientations were recorded in order to determine the extent of occurrence of the α and β modifications of Be_3N_2 and to determine the correctness of the structures found by x-ray diffraction. The diffraction camera constant was calibrated using an evaporated gold foil as a diffraction standard enabling interplanar spacings to be measured and compared with calculated interplanar spacings and structure factors for the two structural modifications. All observed diffraction patterns were indexed and could be accounted for by one of the two modifications confirming the x-ray determined structures (Fig. 3(a-e)). Three-fold symmetry poles were distinguished from six-fold, by the symmetry of the Kikuchi map around each pole, enabling the {111} and {001} poles of cubic and hexagonal structures to be identified. Equiaxed grains 5-10 μm in diameter of both α and β structures were observed, a higher proportion being of the β form. Using x-ray diffraction sample 1 was determined

to consist of 99% β Be_3N_2. The high proportion of grains of the α form found indicates that more material remained untransformed to β during hot pressing than was found by x-rays.[6]

All grains examined were defect free and no intergrowths of the two forms were seen. Small amounts of a dense phase were observed at the triple points and grain boundaries (Fig. 2). No diffraction pattern was obtainable from these regions; it seems likely, however, that they are an impurity phase such as FeSi as reported by Huesby.[6]

III.2. Structure of $BeSiN_2$

The structure of $BeSiN_2$ has been previously determined by x-ray analysis of single crystals to be a partially ordered wurtzite structure.[18] The nitrogen atoms form a hexagonally close packed lattice while the metal atoms Be and Si occupy tetrahedral sites in this lattice (as in the wurtize structure). The result is alternate zig-zag chains of Si and Be filled tetrahedral sites along the [100] direction of the unit cell. This reduces the hexagonal symmetry of the wurtzite arrangement to orthorombic symmetry with a_o = 4.977Å, b_o = 5.747Å and c_o = 4.674Å. Three varients of the ordered structure related by a rotation of 120° about the [001] direction have been found to occur in single crystals. Examination of sample 4 showed that grains consisted predominently of a wurtzite structure but contained large numbers of planar defects which will be discussed later.

Electron diffraction from individual regions of perfect crystal produced sharp fundamental reflections corresponding to a wurtzite structure. Superlattice reflections resulting from the ordered structure were observed and varied from diffuse intensity to sharp well defined

spots in selected area diffraction patterns (Figs. 4(c-d)). A typical region is shown in Fig. 4(a) for a foil zone axis near [001]. A dark field image was taken using the two reflections arrowed and appears in Fig. 4(b). This shows that part of the region contained well ordered domains about 400-600Å across.

Dark field images were subsquently taken in an under and over focused condition using these same reflections in order to determine whether both reflections were from the same ordered varient. The resulting "2-1/2 D image"[19] is shown as a stereo pair in Fig. 5. The relative shift with change of focus of the dark field images of that region of the crystal producing reflection 1 and regions producing reflection 2 produce a pseudo 3D effect.[19] The ordered domains appear to be lying at two different levels within the foil indicating that reflections 1 and 2 arise from two ordered variants of the $BeSiN_2$ structure. The presence of the third ordered variant is suggested by dark regions in the image. This is confirmed by the presence of superlattice reflections from all three variants in the diffraction pattern (Fig. 4(c) labeled 1, 2 and 3).

The remainder of the region has a speckled appearance. The selected area diffraction pattern from a region adjacent to the ordered domains contains diffuse reflections corresponding to the three ordered variants (Fig. 4(d)). This could be due to short range order or the occurrence of small domains of well ordered structure.

These observations are in agreement with the x-ray determined structure of $BeSiN_2$. The occurrence of well ordered regions suggests that the structure may, however, be fully ordered.

III.3. The Structure of the 15R $Be_9Si_3N_{10}$ Polytype

Individual grains of a polytype structure in sample 2 were examined using selected area diffraction and lattice imaging techniques in order to determine the stacking sequence of the close packed planes. On tilting to an (010) orientation the close packed planes lie parallel to the electron beam and thus enabled stacking periodicities of the close packed planes to be examined. The symmetry of the non-central ($\pm$20 ℓ) rows of reflections in the electron diffraction pattern then indicates the unit cell symmetry. The spacing of the spots in the (00ℓ) row of reflections indicates the repeat stacking distance in the close packed direction. The selected area diffraction pattern in Fig. 6 is consistent with prior x-ray results and identifies the region from which it was taken as having a 15R polytype structure.

Periodicities in the close packed direction were examined by phase contrast lattice imaging. In Fig. 7 the repeat block of a region of 15R structure has been imaged using the 000, 003 and 00$\bar{3}$ beams. A regular periodicity of 12.1Å is seen. Direct lattice fringe imaging of the close packed planes (using tilted illumination) shows that each block consists of 5 close packed layers (Fig. 8). The change in fringe contrast every fifth layer suggests a composition and or stacking change occurs every fifth close packed layer (Fig. 8). These observations are consistent with the x-ray determined structure in which a M_2X layer with cubic stacking occurs every fifth layer in the 15R structure.

The appearance of a typical region of sample 2 at low magnification is shown in Fig. 9. the grains are regular in shape and 5-10 µms

in diameter. Many grains exhibited bands of alternate light and dark contrast lying parallel to the close packed planes and few grains were defect free. The regularity of stacking varied from regions of ordered 15R structure containing only isolated faults in stacking (Fig. 8) to highly disordered regions in which the 15R structure was almost completely disrupted (Fig. 10). Disordered regions were easily identified by imaging the block spacing and in highly disordered regions by streaking in the diffraction pattern along the 00ℓ row of reflections. Changes in block spacing in the image indicate a change in spacing of the M_2X layers.

In order to obtain further information about the crystallography of the 15R structure the close packed planes and planes at an angle to the close packed planes were simultaneously imaged. On orienting a grain so that the electron beam was exactly parallel to the [010] direction, it was possible to allow the (0,0,3)-(0,0,15) close packed plane reflections and the $(2,0,\bar{1})$-(2,0,14) reflections from the non-central row of reflections to pass through the objective aperture (Fig. 6). By recombination of these reflections a two dimensional "structure image" was obtained (Fig. 11). The geometrical center of the reflections used was situated on the optic axis of the microscope by electromagnetic beam deflection so as to minimize the effect of spherical aberration on resolution (see Appendix II). A thin region of the crystal was chosen. The focal position of minimum contrast of the carbon layer was selected as a reference point for focus and a through focal series of 40Å intervals of focus was taken. The image shown is defocused 160Å from the reference focus and lies about 500Å

from the edge of the foil. Under conditions similar to these it has been shown that the image obtained has a direct correspondence to a magnified projection of the charge density within the crystal.[20] A periodicity of five close packed planes occurs over most of the area. A periodicity of four close packed planes is observed in the upper right-hand corner indicating a region of intergrown 8H structure. In the region of 15R structure the fourth and fifth fringes are lighter in each block. As the charge density associated with the nitrogen atoms has a periodicity of one close packed layer, this change in contrast is most likely to be due to the siting of the beryllium and silicon atoms in tetrahedral sites. This suggests that the lighter beryllium atoms are sited preferentially in two layers of the structure producing higher contrast in the image. The most probable locations for the beryllium atoms is in tetrahedral sites between the cubic stacked nitrogen atom layers. Tetrahedral sites in these two layers are arranged in the same way as those in cubic stacked nitrogen layers in β Be_3N_2. In one layer all the tetrahedral sites are occupied (composition M_2X). The other layer consists of tetrahedral sites which share a common base with available sites in the next layer and so only half the sites can be occupied (composition MX). The overall composition of these two layers when metal atom sites are occupied exclusively by beryllium atoms is Be_3N_2. The remainder of the structure has a hexagonally close packed arrangement of nitrogen atoms with metal atom sites in a wurtzite arrangements. If these sites are occupied as for the other end member of the series (viz $BeSiN_2$) an overall composition of $Be_9Si_3N_{10}$ is predicted for the 15R structure

in complete agreement with the experimentally determined composition of the 15R structure.

The structural arrangement proposed on the basis of x-ray analysis is graphically confirmed by comparison of an enlarged region of Fig. 11 with a projection of the above structural model in the same orientation, as is shown in Fig. 12. It can be seen that the structure consists of three blocks of identical structure (marked) related by a translation of 1/3[100]. This gives rise to repeat stacking sequence of 15 close packed planes and a unit cell of rhombohedral symmetry. The proposed siting of the Be and Si atoms is also seen to be consistent with fine details of the image.

The agreement is suprisingly good in view of the small number of beams combined to form the image. In order that a true point-to-point resolution be obtained at this level of detail, many more beams would have to be used to form the image. In crystallographically simple structures it has, however, been demonstrated that good agreement between projected charge density and two dimensional images, formed using as few as five beams, can be obtained.[21] It is concluded that the beams used to form the image in Fig. 11 were sufficient to yield a useful approximation to the projected image of the actual crystal structure.

This arrangement of metal atoms enables the 15R structure to be described as a coherent intergrowth of two types of structural block. The first consists of blocks one close packed layer thick which are stacked in a wurtzite arrangement of composition $BeSiN_2$. The second is a block two close packed layers thick having a cubic

stacked nitrogen lattice, of composition Be_3N_2. This is equivalent to the regular insertion of a Be_3N_2 block into a crystal of $BeSiN_2$ structure.

In the 15R structure a Be_3N_2 block occurs every third $BeSiN_2$ layer. Each structural block is electrically neutral and so the number of $BeSiN_2$ layers between the Be_3N_2 blocks may be varied without rearrangement of the atoms for charge compensation. Variation of the number of layers of $BeSiN_2$ structure per Be_3N_2 averaged over a whole crystal varies with crystal composition in a continuous manner from Be_3N_2 to $BeSiN_2$. For integral values of this ratio (0, 1, 2, 3, 4, 5, 6 and 7) ordered arrangements occur, the Be_3N_2 blocks being separated by an integral number of $BeSiN_2$ layers. These ordered structures correspond to the polytype structures βBe_3N_2(4H), 9H, 8H, 15R, 12H, 21R, 16H, 27R [1] of which, except for 16H have been observed by x-ray analysis. For integral values above 7 no ordered structures have been observed. This description of the polytype structures enables the composition of each member of the series to be predicted. The compositions are in complete agreement with those found experimentally confirming the correctness of the phases found along $BeSiN_2$-Be_3N_2 tie line in the Be-SiO-N phase diagram by Huesby[6] (see Chapter IV).

III.4. Twinning and Disorders in the Polytype Structure

The contrast behavior of a region of 15R structure was examined by tilting, Fig. 13. With the electron beam parallel to the [010] direction, contrast was uniform throughout the grain in a bright field imaging mode (Fig. 13(a)). When the grain was tilted about the directions indicated by the arrows, Fig. 13(b-c) alternate dark and light bands

appeared, with the contrast being reversed in Fig. 13(c). This contrast behavior can arise from twins.[22] Differential contrast between twinned regions arises on tilting due to reflections from one twin orientation being more strongly excited than those from the other orientation. Dynamical interaction between the strongly excited reflections and the transmitted beam produces the observed contrast. Selected area diffraction patterns from either side of the boundary and across the boundary confirm that the two regions are in twin relation and that the close packed plane is the twin boundary. In addition to the main twin two thin twin lamelar (L in Fig. 13) occur close to the boundary.

In another experiment a disordered region of 15R structure was tilted as before to produce differential contrast between twins. The region was found to contain a large number of twins. In Fig. 14 the tilted image of the twins is compared with high resolution image of the block spacings in the same area. Associated with each twin interface is a disorder in the regular 15R block spacing. The way in which a twin of this kind arises structurally can easily be visualized.

The 15R structure can be considered as being made up of identical blocks of five hexagonally close packed layers. Each block is related to the adjacent block by a displacement of 1/3[100] as in Fig. 12. This produces a layer of cubic stacking between the blocks i.e., the composition is that of a Be_3N_2 layer. In the twin the displacement relating blocks is in the opposite direction i.e., -1/3[100]. This is equivalent to a 180° rotation of the structure about the [001] direction. A perfect 15R structure is then represented using the

stacking symbols A, B, and C as:

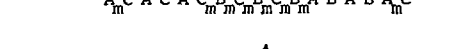

after the notation of Jack.[4]

Changing the stacking sequence of the blocks so that a twin results, the stacking sequence across the twin plane becomes

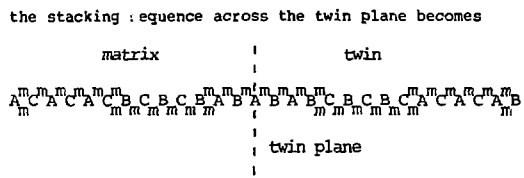

the change in stacking produces an extra layer of hexagonal stacking followed by a cubic Be_3N_2 layer. This is equivalent to the insertion of one block of six close packed layers instead of five or one extra layer of composition $BeSiN_2$. From this it can be seen that disorders in the 15R structure are closely related to twinning. In a similar manner, if one close packed $BeSiN_2$ layer is removed, a twin relationship results. The stacking sequence across the twin boundary is then

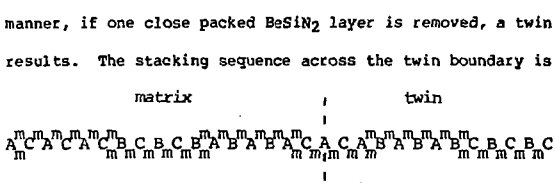

The insertion or removal of two extra planes does not produce a twin. Only blocks containing a even number of close packed planes result in a twin.

In this way twins can arise in all the rombohedral polytypes by the inclusion of a block consisting of an even number of close

packed planes. This process must locally change the composition i.e., the shear is non-conservative. In the hexagonal polytypes each block is the twin of the adjacent block as they consist of an even number of close packed planes. Insertion or removal of one $BeSiN_2$ close packed layer to produce a block consisting of an odd number of close packed layers, locally removes this twin relationship over a region of crystal two blocks wide. Each change in block size results in a local change in composition due to the change in the periodicity of the Be_3N_2 layers in the structure. It is clear from this model of the twins that local variations in composition, disordering of the structure and the resulting twins are inseperable. Also, the twins are of the type described by Anderson and Hyde, i.e., chemical twins as rather than mechanical twins.[23]

Inclusion of more and more blocks of the next number of the series into the 15R structure results in more frequent twinning of the structure. the composition of the structure approaches that of the next member of the series. Finally, twinning every block occurs and and next member of the series results, having a hexagonal structure. An example of this kind of intergrowth was observed by imaging the block spacings across a single grain as shown in Fig. 15. A regular spacing of 12.1 Å occurs in the top left-hand corner. The spacing of the spots in the electron diffraction pattern from this region confirms that this is a region of 15R structure (Fig. 16(a)). Optical diffraction from this area of the image produced single sharp diffraction spots indicating that the region is fully ordered (Fig. 16(d)). However, on crossing the grain the structure becomes disordered. The selected area

diffraction pattern takes using a 1μ aperture centered on the disordered region contains reflections corresponding to both the 15R and 8H structures (Fig. 16(b)). Optical diffraction patterns (see Appendix II) from this region using a 500Å diameter aperture show that disordering of the blocks occurs even at this scale (Fig. 16(e)). By taking optical diffraction patterns from regions of the image 100Å across using a smaller aperture, it was possible to discern regions of well ordered 15R and 8H block periodicity within the disordered region (Figs. 16(g-h). Further across the grain a region of well ordered 8H structure occurs (bottom right of Fig. 15), as indicated by the electron and optical diffraction patterns (Fig 16(c)(f)). The transition from well ordered 15R structure to well ordered 8H structure occurs over a distance of about 0.5μ. The corresponding composition change is then $Be_9Si_3N_{10}$ to $Be_5Si_2N_6$. The transition occurs via a region of mixed 15R and 8H structural blocks. It seems likely that the transitions from one member of the polytype series to the next occur in the same manner when local fluctuations in composition arise within a grain. Grains with a uniform composition throughout will then consist of a proportional mixture of blocks of two adjacent polytype structures. Grains of completely ordered structure will only occur at the exact polytype compositions.

III-5. Twin Terminations

A number of twins made visible by tilting were seen to terminate within grains at an incoherent interface (Fig. 17(a-b)). The shape of the termination when tilted from the 010 foil orientation indicates

that it is inclined to the foil surface. Other terminations examined were almost parallel to the foil normal, [010].

Imaging the block spacing in an [100] foil orientation was done so as to examine the terminations (Fig. 18(a)). The change in block spacing (A) produces a twin; the second change in block spacing removes the twin reflection (B). The disorders terminate at the region in dark contrast indicating the termination of the twin. The region in dark contrast corresponds to the incoherent interface of the twin.

Inclination of the interface is indicated by broad depth fringes in the boundary image. Taking a foil thickness of 1000-2000Å an inclination of 21-37° to the [100] direction was estimated from Fig. 19. The boundary, therefore, lies roughly in the ($\bar{1}20$) or (120) planes.

Figures 18(b-c) show the change in contrast with diffracting conditions of g = 040 (s = 0) and excitation of the 00ℓ systematic row of reflections (s = 0 for 0,0,15). In Fig. 18(b) (g = 040) the termination appears to consist of eight dislocations lying in the close packed planes along the [210] or [$2\bar{1}0$] directions (30° from the [100] direction). For g = 001 the dislocations are invisible. From the g·b = 0 criterion for the invisibility of dislocations it can be deduced that the Burgers vectors of the dislocation terminating the twin lie in the close packed plane. The $\pm$003 reflections as well as the transmitted beam were unavoidably allowed to pass through the objective aperture resulting in the fringes seen in Fig. 18(c). Complicated wavy fringe contrast is seen in the region of the termination, however, little significance can be attached to the form

of the image due to the complex and uncertain imaging conditions in this region of the crystal.

Terminating twins were examined by tilting grains so that the close packed planes lay at an angle to the electron beam. For several reflections the dislocations were visible and could be seen to terminate complex stacking fault fringe contrast arising from the stacking disorders that produce the twins, Fig. 20. It was possible to tilt other grains exhibiting the same contrast to an [001] orientation, so that the close packed planes were perpendicular to the electron beam. A region of such a grain in [001] orientation has been imaged in Fig. 21. Three sets of dislocations are visible lying predominantly along [010] [210] and [$2\bar{1}0$] directions 60° apart in agreement with the previous observations of dislocations at terminating twins. The corresponding diffraction pattern shown in Fig. 21(d) has three-fold symmetry as indicated by the Kikuchi lines. The area was, therefore, identified as a region of predominantly rhombohedral polytype structure. The strong appearance of the 120, 200 and $1\bar{2}0$, reflections forbidden for rombohedral polytypes, cannot be attributed to double diffraction. Their occurrence due to second Laue zone effects as a result of the thinness of the crystal can also be eliminated as the reflections were persistant in thick regions of the grain. This suggests that elongation of reciprocal lattice points due to thin disorder regions of stacking has occurred producing reflections from the next Laue zone. This is further supported by the appearance of complicated fringe contrast that probably arises from the over lap of a number of stacking disorders in Fig. 21(c). The abrupt change in fringe

contrast on crossing dislocations 1, 2, 3 and 4 suggests that the dislocations terminate stacking disorders, and hence twins, within the crystallite.

The same area has been imaged using the two beam conditions $g = 040$, $g = 320$ and $g = 3\bar{2}0$ respectively in Figs. 21(a-c). Dislocation 1 is invisible for $g = 040$ and dislocation 2 is invisible for $g = 3\bar{2}0$. The previous experiment indicates that the dislocations terminating twins have a Burgers vector lying in the close packed plane. From the $g \cdot b = 0$ criterion for no contrast it can be deduced that the direction of the Burgers vectors of dislocations 1 and 2 are $[100]$ and $[2\bar{3}0]$ respectively. Dislocations 3 and 4 exhibit weak contrast for $g = 320$ and $g = 040$ respectively and appear to consist of 2 or more overlaping dislocations. Even if $(g \cdot b) \approx 0$ weak contrast may still arise due to the elastic anisotropy of the structure causing $(g \cdot (b \times u)) \neq 0$. Such would be the case if the dislocations did not lie in the close packed plane (u = a unit vector in the direction of the dislocation line). Burgers vectors in the $[230]$ and $[100]$ directions may then be assigned to dislocations 3 and 4 respectively.

A plausible dislocation model for the twin/disorder terminations can be established by considering the stacking of the close packed planes. In the matrix, each block of five hexagonally close packed layers is related to the adjacent one by a displacement of the type $1/3\langle 100\rangle$, equivalent to the translation between close packed stacking positions, $1/3[100]$, $1/12[2\bar{3}0]$, $1/12[\bar{2}30]$. In the twin a translation of $-1/3\langle 100\rangle$ relates the blocks. The change from a block stacking of $+1/3\langle 100\rangle$ to $-1/3\langle 100\rangle$ across the coherent twin boundary produces

a stacking disorder, as described before, in the form of a block of 4 or 6 close packed layers. The (010) projection of a terminating twin three blocks wide is shown in Fig. 22. It can be seen that mismatch of the stacking of the close packed planes occurs over only two blocks and that the cubic stacked (M_2X) layers are displaced by one close packed layer spacing in the twin. This displacement results from the stacking disorders which accommodate the twin at the coherent boundaries. At the incoherent interface of the twin the close packed layer stacking matches up to the last layer of the disordered block. The stacking mismatch in the next layer has then to be accommodated by a dislocation of Burgers vector -1/3[100]. This matches stacking for a further five layers after which another partial of burgers vector +1/3[100] is required to accommodate the stacking mismatch in the next block. The stacking in the third block is then the same in the twin and the matrix. The mismatch could also be accommodated by a displacement of +2/3[100] of the first block and +1/3[100] of the second block. This, however, would be energetically less favorable (because of the larger $|b|^2$) and so has been ruled out.

The atom positions and displacements in the region marked in Fig. 22 are shown in Fig. 23. The diagram represents an (010) planar section of the terminating twin. On the left the positions of the next layer of nitrogen atoms above and below the section plane have been drawn in to show the tetrahedra. They are omitted in the rest of the diagram to avoid confusion. The structural blocks in the matrix are indicated by the dotted out lines on the left. In block 1, layers 1-5, the atoms are undisplaced in the twin. In the next block,

block 2, atoms in the twin are displaced to the left by -1/3[100]. This brings the atoms at the twin matrix interface too close, producing a compresive distortion of the lattice. In the next block, block 3, atoms in the twin are displaced by 1/3[100] to the right. This moves atoms at the interface too far apart resulting in a region of expansive distortion of the lattice. The stacking then again matches across the interface, in the next block and the sequence may repeat or as in Fig. 22, terminate in a further disorder. It can be seen that these atomic displacements create the twinned structure by twinning the stacking of the nitrogen atoms and metal atoms in downward pointing tetrahedral sites. However, metal atoms in the M_2X cubic stacked layer in upward pointing tetrahedral sites are not moved to their correct positions in the twin by these displacements. Metal atoms in these sites would have to move to the newly created non base sharing tetrahedral sites in the twin (indicated by the curved arrows) by some diffusional process. Indeed diffusional rearrangement of beryllium and silicon atoms would be required to create the Be_3N_2 and $BeSiN_2$ layer structure in the twin. The structural arrangement of atoms in the twin is then identical to that in the matrix with the exception of a 180° rotation about the [001] direction and a displacement of one close packed layer spacing upwards. The structural blocks in the twin are outlined on the right in Fig. 23.

The structural rearrangement at the twin/matrix interface can thus be described by a synchronous shearing and diffusion process. The mismatch at the incoherent interface may be accommodated by dislocations with the experimentally determined Burgers vector of

1/3 (100). Mismatch occurs in two out of every three blocks and is accommodated by two partial dislocations of opposite sign. This creates regions of alternate compression and expansion followed by perfect matching at the interface, repeating every three blocks as shown in Fig. 24. (The dotted line marks the new position of the M_2X layer in the twin.) In order that matching of stacking occurs at both of the coherent boundaries, the twin must be an integral multiple of three blocks wide. Examination of the twin imaged in Fig. 21 shows that it is exactly 24 blocks wide. An array of 8 pairs of partials is thus required to accommodate the termination, one pair of partials per three blocks. The contrast seen in Fig. 21(b) arises from the distortion of the lattice produced by alternate expansion of compression of the lattice, producing eight single line images.

Other twin terminations were more complex, terminating several disorders in the structure. It seems probable that a similar model could also apply to such terminations. In all the terminations examined by high resolution imaging of the block spacings, it was found that the number of fringes either side of the termination was the same. This suggests that the number of M_2X layers remains constant in ratio to the number of MX layers producing no net composition change at the twin terminations. Such terminations, however, if mobile at hot pressing temperatures, would enable an M_2X layer to propagate in the [001] direction. This movement permits a disordered structure to then order into a perfect polytype structure. The driving force for the interfacial movement being the interaction forces between

M_2X layers which order them into periodic structures. The origin of such forces will be considered in more detail in the discussion.

III-6. Faults in the $BeSiN_2$ Structure

Examination of grains in sample 4 showed that many grains consisting predominantly of a $BeSiN_2$ structure contained a high density of structural irregularities. Two types of planar defect were observed. the first consisted of defects which lay in the close packed planes producing fringe contrast characteristic of stacking faults or thin precipitates when tilted so that the incident beam was at an angle to the fault plane. The faults resulted in a continuous streak in the [001] direction in reciprocal space indicating the faults were one or two close packed layers thick. The second kind of planar defect was observed to lie on curved planes, at an angle to the close packed plane. These again gave rise to fringe type contrast for several diffracting conditions: The results of Section III-2 showed that the ordering of the Be and Si atoms is incomplete or consists of small domains of all three ordered varients. Macroscopically the crystal structure of $BeSiN_2$ grains can, therefore, be considered as being disordered possessing the full hexagonal symmetry of a wurtzite structure. Drum[24] considered the contrast arising from such faults in a wurtzite structure.

Reasonable displacement vectors for faults in the close packed planes would be translations (P) between stacking positions A, B and C, lying in the close packed planes; a translation (1/2 C) of one close packed layer spacing perpendicular to the close packed planes and a combination of these two displacements P + 1/2 C (after Drum).

The displacement P + 1/2 C corresponds to the translation between nitrogen atoms in adjacent close packed planes.

Isolated faults of both type were imaged using several different diffracting conditions in order to determine their fault vectors (Fig. 25). The faults in the close packed planes were visible for g = 002, $\bar{2}0\bar{1}$, $\bar{2}00$, $\bar{4}00$, and $\bar{6}00$ and invisable for g = 320. Using the criterion g·R = integer for visibility, a displacement vector of 1/2 C (R = 1/2[001]) can be eliminated as the faults are visible for g = $\bar{2}00$ and g = $\bar{4}00$. Two types of fault consisting of P vectors alone can arise. The first is an extrinsic fault which is produced by a shear on two adjacent planes of total fault vector -p+p. As this is a lattice vector such a fault could not be detectable by diffraction contrast and so can be eliminated. The second possible fault consisting of P vectors is an intrinsic fault produced by a single shear of P (R = 1/3[100]). The appearance of the faults for g = $\bar{2}00$, g = $\bar{4}00$ and the weak appearance for g = $\bar{6}00$ and disappearance for g = 320 suggest the presence of a P component to the fault vector. It is not possible, however, to distinguish between the three possible P vectors by fault contrast as they differ only by a lattice vector. It is also difficult to distinguish between faults of the type P and P + 1/2 C as pointed out by Drum.[24] However, as can be seen from Table I the phase factor introduced by faults of displacement vector P for g = $\bar{2}00$ and $\bar{2}0\bar{1}$ is -2/3 π in both cases. For faults of displacement vector P + 1/2 C, α = -1/3 π for g = $\bar{2}0\bar{1}$ and α = 2/3 π for g = $\bar{2}00$. The contrast of the outer fringe is dependent on α, i.e., dark for α = -1/3 π, -2/3 π and light

for $\alpha = +1/3\ \pi, +2/3\ \pi$.[15] A change in contrast of the outer fringe in images from $g = \bar{2}00$ to $g = \bar{2}0\bar{1}$, therefore, occurs only if a component 1/2 C is present in the fault vector. The appearance of a dark outer fringe for $g = \bar{2}0\bar{1}$ (Fig. 25(b)) and a light fringe for $g = \bar{2}00$ (Fig. 25(c)) indicates the presence of a component 1/2 C in the fault vector. The probable displacement vector of the faults lying in the close packed planes is thus of the type P + 1/2 C, i.e., the faults shown in Fig. 16, R = 1/3[203].

The complete disappearance of faults for $g = \bar{6}00$ and $g = 002$ should occur for R = 1/6[203] but is not observed. The weak appearance of fault fringes for $g = \bar{6}00$ and complete disappearance for $g = 320$ suggests that the displacemnt in [100] is not exactly 1/3[100] but such that $g \cdot R$ = integer ∓ 0.02 for $g = 320$ and $g \cdot R \neq$ integer ∓ 0.02 for $g = \bar{6}00$ so that incomplete disappearance occurs for $g = \bar{6}00$. These results follow from the criterion that $g \cdot R$ = integer ± 0.02 for complete disappearance of faults as demonstrated by Booker and Howie.[26] The strong appearance of the faults for $g = 002$ implies that the [001] component of the displacement vector is not 1/2 C (R = 1/2[001]) but some non integral value. These results and the observation of strain contrast associated with some of the faults (bottom right of Fig. 25(a)) imply some distortion of the lattice and/or change in interatomic spacing is associated with the formation of the faults.

The faults lying on curved planes were visible for $g = 002$ and $g = \bar{2}0\bar{1}$ and invisible for $g = \bar{2}00$, $\bar{4}00$, $\bar{6}00$ and 320 (Fig. 25). These observations are not consistent with any simple displacement

vector for the faults. However, the wurtzite structure is non centrosymmetric and exists in two forms; one in which all upward pointing tetrahedral sites are occupied by atoms and the other in which all downward pointing sites are filled. A boundary between the two forms would be visible for all reflections from noncentrosymmetric planes, i.e., planes not perpendicular to the close packed planes with indices uvw where $w \neq 0$. The boundary would be invisible for $g = u, v, o$. The faults lying in curved planes, therefore, exhibit contrast consistent for enantromorphic boundaries in a wurtzite structure. This result was further substantiated by dark field imaging of faulted grains using $\pm g = 002$ with several other beams simultaneously strongly excited. The violation of Friedel's law for these noncentrosymmetric reflections gives rise to different intensities from the two enantiomorphic forms[27] (Fig. 26). A thin area of the specimen was selected to reduce the effects of inelastic scattering, which reduces the difference in contrast between the two forms. The high voltage microscope (650 kV) was used to further reduce the effects of inelastic scattering and to excite more reflections in the multibeam situation. Contrast from the two forms reversed on changing the sign of g and it can be seen that parts of the faults in the close packed planes are also enantiomorphic boundaries.

The density of faults in the close packed planes varied greatly from grain to grain. Figure 27 shows a typical region of a grain containing a moderate density of faults, in an (010) orientation. A number of faults terminate within the grain, fault A terminating at both ends. The terminations are characterized by strain contrast typical of a dislocation inclined within the foil. Some faults also

exhibited alternating black-white strain contrast along the length of the fault B. The faults commonly occurred in pairs spaced about 40-50Å apart C. Contrast between the faults (C) is suggestive of distortion of the matrix structure in this region.

In another grain of (010) orientation an array of closely spaced faults has formed, 20-50Å appart (Fig. 28). The faults cover most of the grain with the exception of the region to the right. Electron diffraction from the fault free region shows it has a $BeSiN_2$ partially ordered wurtzite structure. the faults again appear to have preferentially formed in pairs. A selected area diffraction pattern from the faulted region exhibited a continuous streak in the [001]* direction. A dark field image taken using the streak clearly showed the faults in bright contrast (Fig. 28(b)).

In Fig. 29 a series of images across a similar grain are shown. A very high density of faults are seen edge on. The density of faults increasing from top to bottom, along the direction of the arrows. In the top image to the left, the grain is fault free. A selected area electron diffraction pattern from this region again indicates it has a $BeSiN_2$ structure (Fig. 30(a). A SAD pattern taken with the intermediate aperture centered on the middle region contained a continuous streak in the [001]* direction (Fig. 30(b)). In an SAD pattern from the lower region, a continuous streak is again observed; only seven evenly spaced maxima in the streak occur from the transmitted beam up to and including the reflection from the close packed planes (Fig. 30(c)). The maxima are suggestive of a preferential periodicity of seven close packed plane spacings in the lattice or 16.4Å.

By using the electron microscopy images in Fig. 29 as a diffraction grating for a laser light source the periodicity and spacing of the faults were examined (see Appendix II). Using a medium sized aperture, iluminating an area of about 500Å in diameter with respect to the crystal, a continuous streak in the optical diffraction pattern was observed. Examples of optical diffraction patterns taken from selected areas of the top, middle and bottom images are shown in Figs. 30(d-f) respectively. Maxima occur in the streaks, increasing in distance from the transmitted beam in going from top to bottom. This would indicate that the faults are almost randomly spaced only with a decreasing preferential spacing in going from top to bottom of Fig. 29. By using a smaller aperture (200Å effective diameter) isolated regions of regularly spaced faults were detected giving distinct reflections in optical diffraction patterns. The camera length of the optical bench was determined, using a standard grating in order to determine the spacing of faults from the spacing of reflections in the optical diffraction patterns. Using this technique three distinct regular fault periodicities were found. Examples of optical diffraction patterns are shown in Figs. 30(g-i). The positions of the aperture (1, 2 and 3 respectively) are marked in Fig. 29. The experimentally measured fault spacings were 21.1Å, 16.3Å and 21.1Å from regions 1, 2 and 3. These correspond to periodicity of 9, 7 and 6 close packed layer spacings.

Assuming each fault in a regular array has the experimentally determined displacement vector of 1/6⟨203⟩, the structure of a regularly faulted region can be deduced. The effect of the displacement vector

1/6⟨203⟩ on a perfect wurtzite structure is to shear one layer of nitrogen atoms to the position of nitrogen atoms in the next close packed plane. This effectively removes one layer of nitrogen atoms from the structure leaving an excess of metal atoms in a cubic stacked nitrogen lattice. The shear in creating a cubic layer forms non base shearing tetrahedral sites capable of accommodating the excess metal atoms. The composition of the layer is then M_2X and has the same structure as a single M_2X layer in a polytype structure (Fig. 31(a-b). The structure produced by a regular array of faults is thus identical to that of a polytype structure. The regular periodicities of 9, 7 and 6 close pack layers observed in Fig. 29 corresponding respectively to thin domains of 27R, 21R and 12H structures.

These structures in which a regular arrangement of faults accommodates changes in composition are analogous to the so called shear structures observed in complex metal oxides.[28,29] In such oxides two dimentional arrays of "crystallographic shear faults" transform the basic oxide structure to a structure of different composition and unit cell dimensions. The unit cell dimensions depend on the spacing between shear faults and as the spacing varies with composition a complete homologous series of structures occurs as composition changes. The above results suggest that in the $BeSiN_2$-Be_3N_2 system a one dimensional array of crystallographic shear faults (R = 1/6[203]) form in the ordered wurtzite $BeSiN_2$ structure as the composition changes. These faults produce a series of structures in which only one unit cell dimension is changed with composition, i.e., the observed polytype series.

IV. DISCUSSION

IV.1. Stoichiometry and Polytype Structures

The observations made in the previous sections and their interpretation confirm the correctness of the $Be_xSi_yN_z$ polytype structures as determined by Thompson using x-ray analysis.[5] The way in which these structures arise can easily be described as a regular faulting of the $BeSiN_2$ structure to accommodate excess beryllium atoms. Each fault of displacement vector 1/6⟨203⟩ having a component out of the fault plane, effectively removes one close packed layer of nitrogen atoms leaving an extra layer of metal atoms. The tetrahedral metal atom sites in the cubic stacked nitrogen layer created no longer share bases with tetrahedral sites in the next close packed layer. Both upward and downward pointing tetrahedral sites can then be occupied enabling the extra metal atoms to be accommodated (Fig. 31(a-b)). The extra metal atom site per nitrogen atom in the fault makes them favorable sites for lower valency Be^{2+} atoms as this results in local change compensation within the structure and so reduces the electrostatic imbalances between fault and matrix. Complete charge compensation can be produced if all metal atom sites in the M_2X layer and the next MX layer are occupied by beryllium atoms to form a block two close packed layers thick of composition Be_3N_2, as suggested by the results of Section III.3. In this way an excess of beryllium atoms can be accommodated in the $BeSiN_2$ structure.

For small deviations from the exact $BeSiN_2$ composition towards a composition of Be_3N_2, isolated faults of this kind can accommodate the excess of beryllium atoms; their density increasing as larger

deviations from stoichiometry occur. At some composition along the $BeSiN_2$-Be_3N_2 tie line the faults can no longer be considered as being isolated and start to interact with adjacent faults due to their high density and hence close proximity. Regular arrays of faults then arise so as minimize their interaction energy, tending to form the polytype structures. The overall composition of a region of faulted structure is determined by the number of $BeSiN_2$ close packed layers per fault. Clearly perfectly regular faulting can only occur for integral values of this ratio and hence for specific compositions and metal to non metal atom ratios. At intermediate compositions, intermixed fault spacings will occur producing irregularly twinned structures, as described in Section III.4.

The results of Section III 6 suggest that the first member of the polytype series is 27R as found by x-ray analysis.[5] This corresponds to a fault spacing of nine close packed layers, although interaction probably extends over larger distances as suggested by the common occurrence of fault pairs 30-40Å apart. The anomalous absence of evidence for a 16H polytype in Section III-6 and x-ray diffraction patterns[5] remains to be explained. It is possible, though, that such a regular spacing of faults (8 close packed layers) has an unfavorable interaction energy, preventing its formation. All other regular fault arrangements have been observed using x-ray techniques.

At compositions approaching Be_3N_2, $BeSiN_2$ layers can no longer separate all the faults. The structure produced by such an arrangement

is that of β Be_3N_2 consisting of two cubic stacked Be_3N_2 fault layers displaced with respect to each other to form a hexagonal unit cell.

Each Be_3N_2 fault layer resembles a block two close packed layers thick of β Be_3N_2 structure in a $BeSiN_2$ matrix. By a proportionate summing of the extreme members of the series in each polytype, a composition for each polytype can be predicted (Table II). The predicted compositions are found to match those found experimentally. Adopting a simplistic view of each polytype structure by considering them to be made up of non interacting layers of β Be_3N_2 and $BeSiN_2$ structures, stacked in the appropriate manner, a prediction of the unit cell dimensions in the [001] direction can be made (Table II). Superficially the agreement with experiment seems good but it is found that the linear variation with composition predicted is not obeyed. A more realistic view in which interatomic forces and matching of atomic positions across the block interfaces are considered may account for this. Indeed some evidence was found for elastic distortion of the matrix being associated with isolated faults and fault pairs and also a change in close packed layer spacing being associated with fault formation (Section III.6). It is conceivable also that such an elastic distortion could play an important role in fault interactions and so polytype formation.

IV.2. Formation of polytype structures

The occurrence of shear faults which change the coordination of polyhedral atom sites to incorporate excess interstitial atoms has been found to be a common phenomenon and recently has received much attention.[28-30] The way in which such faults are introduced

into a structure and subsequently form ordered arrays is not well understood.

The observation in non stoichiometric $BeSiN_2$ of isolated faults extending across grains and also terminating within grains suggests a shear mechanism is responsable for their formation. It is possible that enantiomorph boundaries form preferential nucleation sites for the shear faults. The arrangement of metal atom sites across an euantiomorphic boundary is such as to favor their occupation by beryllium atoms to reduce electrostatic imbalances across the boundary. Segregation of the beryllium atoms then favors shearing of the nitrogen lattice to produce a cubic stacked Be_3N_2 composition layer. Some circumstantial evidence for this is found in the close association of faults and enantiomorphic boundaries (Fig. 27).

Once formed a fault could then extend across a grain by a synchronous shearing of the nitrogen lattice and diffusion of interstital metal atoms. The cooperative movement of a large number of atoms would be required to produce a single fault in the $BeSiN_2$ structure or a reverse shearing of the Be_3N_2 structure to produce a single $BeSiN_2$ layer. Such considerable structural rearrangements would, however, seem feasible due to the high hot pressing temperature (1800°C).

Once formed, the rearrangement into regular configurations of faults, which are spaced closely enough to interact, requires sideways [001] movement of the faults. A possible mechanism for such movement is the propagation of twin determinations at hot pressing temperatures. Another possibility is the nucleation of a new more favorable arrangement

of faults at some point in a grain. These could then grow, consuming the existing faulted structure. Some evidence for such a mechanism is seen in Fig. 28 in which an irregular fault arrangement is seen to terminate within a grain being replaced by a more regular and arrangement of faults at A. Such mechanisms are, however, somewhat speculative. Hot stage electron microscope experiments to observe fault formation and ordering may provide more information about such mechanisms.

The simularity of the transformations occurring in Be, Si, N compounds to the phenomena of crystallographic shear in complex oxide structures is unmistakable. Also a analogy can be drawn between the formation of non conservative antiphase boundaries in Ni_4Mo[34] and shear type transformations in metals. However, further work is clearly required to characterize the exact nature of the transformations that occur as the composition of the wurtzite structure is changed.

IV.3. Polytypes in Other Sialon Systems

Similar polytype series to that in the $BeSiN_2$-Be_3N_2 system have been reported in other Sialon systems.[4] In the Be-Si-O-N system an almost identical series of polytypes occur for compositions BeO-Be_3N_2. Both nitrogen and oxygen atoms form the close packed lattice, and beryllium atoms occupy tetrahedral metal atom sites. X-ray analysis has identified the arrangement of non metal and metal atoms as being the same as in the $BeSiN_2$-Be_3N_2 series. The series may be described as in the $BeSiN_2$-Be_3N_2 system as the faulting of a wurtzite structure (BeO) to accommodate changes in composition along the BeO-Be_3N_2 tie line. Description of the polytypes as intergrowths of blocks of BeO

and β Be_3N_2 structure in an analogous manner to the $BeSiN_2$-Be_3N_2 series allows the composition of each polytype to be correctly predicted (Table III). A prediction of unit cell dimensions, again assuming no interaction between structural blocks, shows better agreement with experiment than found in the $BeSiN_2$-Be_3N_2 system (Table III), a linear variation in the c unit cell dimension occurring with composition.

Identical polytype phases in the two systems were found to extend along the same lines of constant metal to non metal atom ratio in the Be-Si-O-N system (Fig. 1). Continuous solid solutions between each polytype, however, were not found. It is possible that polytype structures consisting of more complex structural intergrowths occur in this region of the phase diagram. High resolution electron microscopy of samples of these materials should help establish this point.

Extensive polytypism similar to that in the Be-Si-O-N system also occurs in the Si-Al-O-N system at AlN rich compositions, only with the role of metal and non metal atoms reversed. Again their description as faulted versions of the wurtzite structure (AlN) is possible wherein extra non metal atoms are accommodated at sites with a favorable coordination created by the faults.

In a more complex Sialon system (e.g., Mg-Si-Al-O-N) polytypes with differing atomic structures and unit cell dimensions have been detected, using x-ray analysis, in a single plane of constant metal to non metal atom ratio.[31] Using the concept of coherent intergrowth of layers of differing structure and composition this observation may be rationalized as follows. If the polytypes are made up of more

than two structural blocks each incorporating specific ratios of each element in a favorably coordinated arrangement long period structures may arise. Variations in composition maintaining metal to non metal atom ratios but changing the proportion of specific elements would then result in different proportions of each type of block. The stacking of blocks would then accommodate the composition changes. Such changes in block stacking would result in several different polytypes in a single plane of constant metal to non metal atom ratio in the system. Structurally analogous composition dependent polytypes have been reported in the barium ferrite layer structures[32,33] High resolution transmission electron microscopy should again prove useful in confirming or disproving this hypothesis.

CONCLUSIONS

The main results of this investigation can be summarized as follows:

(1) The atomic positions of metal and non-metal atoms in the $BeSiN_2$-Be_3N_2 polytype structures derived from x-ray data are confirmed by real space high resolution microscope studies.

The results also suggest that beryllium atoms are preferentially sited in cubic stacked layers.

(2) The polytypes may be described in terms of regular faulting of the ordered wurtzite $BeSiN_2$ structure. Each fault (displacement vector 1/6(203)) creates a layer of cubic stacked nitrogen atoms in which tetrahedral metal atom sites no longer share bases. This allows an excess of beryllium atoms to be accommodated in the structure. For a small excess isolated faults occur, their density increasing as the beryllium content increases. At high densities the faults interact and so form regular arrays for specific compositions.

(3) Each fault may be considered as a coherent layered intergrowth of β Be_3N_2 in a $BeSiN_2$ matrix. This model allows the currect composition of each polytype as well as other prominent crystallographic features to be directly predicted.

ACKNOWLEDGEMENTS

The author wishes to express his gratitude to Professors Gareth Thomas and K. H. Jack for their co-operation and encouragement throughout the course of this work. Appreciation is also extended to Professor J. A. Pask and Professor H. R. Wenk for their critical review of the manuscript. In addition the author is grateful to Dr. L. J. Gauckler, Max-Planck Institut fur Metallforschung, Stattgart, for providing the samples.

Special thanks are due to Dr. David R. Clark for his guidence throughout the course of this investigation and for the many illuminating discussions which stirred my mind. Thanks also to Dr. Ronald Gronsky for his assistance in the final preparation of the manuscript. Thanks to Carolyn Gosnell for her efficiency in keeping the microscopes running through thick and thin. Finally the author thanks all his friends and colleagues for providing an atmosphere conducive to pleasurable study.

I gratefully acknowledge the assistance of the support staff of the Lawrence Berkeley Laboratories and the financial support provided by the U. S. Energy Research and Development Administration through the Lawrence Berkeley Laboratories.

Acknowledgement is also due to the National Science Foundation for partial funding of this work.

APPENDIX I. CHOICE OF UNIT CELLS

The unit cells reported in the literature[15-18] to describe both the Be_3N_2 and $BeSiN_2$ structures are as follows:

α Be_3N_2 cubic $a_o = 8.15\text{Å}$

C rare earth structure close packed planes (111)

β Be_3N_2 hexagonal $a_o = 2.842\text{Å}$, $c = 9.706\text{Å}$

Close packed planes (00.1)

$BeSiN_2$ orthorombic $a_o = 4.977\text{Å}$, $b_o = 5.747\text{Å}$

$C_o = 4.674\text{Å}$

Ordered wurtzite close packed planes (001) b_o lies in the close packed plane along tetrahedra edges.

For convenience a unit cell with the same base vectors as for $BeSiN_2$ was chosen to describe the polytype structures, viz, $a_o = 4.9\text{Å}$, $b_o = 5.7\text{Å}$, and c_o a variable multiple of close packed layer spacing. This enables all the polytype structures to be described using the same base vectors for the unit cell. The unit cell described in this way does not reflect the full symmetry of each polytype, which may be romberhedral or hexagonal depending on the stacking of the close packed planes.

APPENDIX II. THE THEORY AND PRACTICE OF LATTICE IMAGING

When two coherent point sources of light are allowed to interfere, fringes are produced as in the Young's fringes experiment. In an analogous way the combination of two diffracted beams in the electron diffraction pattern of a crystal can produce a fringe image (Fig. 32). The spacing of the fringes is inversely proportional to the separation of the two reflections used to form them. If the transmitted beam and one diffracted beam is used, the periodicity of the corresponding diffracting lattice planes in the crystal is reproduced as a set of fringes in the magnified image. Allowing additional diffracted beams to pass through the objective aperture provides additional information about the crystals structure in the fringe image.

The way in which the diffracted beams contribute to the fringe image depends on the relative phases of the diffracted beams. The phases in turn are determined by the orientation, thickness, internal structure and perfection of the crystal as well as the aberrations and focusing of the objective lens. Exact control of all these parameters is required to produce an image that is truely representative of the crystal's structure, e.g., dynamical calculations indicate that at 100 kV two dimensional "structure image" contrast can be directly interpreted in terms of the object only when the specimen is no thicker than 150Å and the objective lens is set at ~500Å defocus.[35] In order that these factors should have a minimum effect on the image, optimum performance of the microscope must be achieved. Theory and practice have established that use of the following procedures provides a means by which reproducable images may be most conveniently obtained.

Instrumental Considerations

Clearly the microscope must be capable of the required resolution levels, typically 3.5Å point to point at 100 kV. The use of higher accelerating voltages can improve resolution significantly.[36] The electron source must provide an electron beam of high brightness and coherency to facilitate focusing of the image at high magnifications (500,000x) and convenient recording of the image. The use of pointed filaments and high efficiency fluorescent screens are thus desirable. Precise control of specimen orientation is necessary in order that the correct diffracting conditions in the area of interest may be obtained. For this a biaxial goniometer stage is essential. In addition to these requirements careful and frequent maintainance of the microscope is necessary, including frequent alignment of the optical column, to ensure optimum performance.

Specimen

The requirement of very thin foils for fringe and structure imaging means that care must be taken in specimen preparation and selection of areas for examination. Any factors such as image instability due to charging in ceramic specimens or contamination of the foil surfaces can result in degredation of resolution in the recorded image. Every precaution should be made to avoid these effects by coating specimens with a thin conducting layer of carbon and the use of anticontamination devices.

Technique for Obtaining Lattice Images

1. In SAD Mode Tilt to Desired Orientation. Two types of orientation are commonly used for lattice imaging.

(a) A Systematic row of reflections in a which a single row of reflections is strongly excited in the diffraction pattern. The image will then consist of a parallel set of fringes corresponding to periodicities in the crystal producing the reflections used to form the image.

(b) Symmetrical or zone axis orientation in which all reflections from a low index zone are excited and so can then be combined to form a two dimentional image of periodicities in the crystal.

2. Positioning of the Optic Axis. The effect of spherical aberrations in the objective lens in reducing resolution and on the relative phases of diffracted beams and hence contrast in the image increases with the distance of the diffracted beams from the optic axis. To minimize this effect the extreme reflections used to form the image are positioned so that they are equidistant from the optic axis, by using the dark field deflection system, as shown in Figs. 33 (b,c). For symmetrical beam images no deflection is required as the optic axis already lies at the center of the reflections, i.e., at the transmitted beam (Fig. 33(a)). For imaging using a non symmetrical set of reflections, beam tilting will be required (Fig. 33 (b,c)).

3. Selection and Positioning of the Objective Aperture. Increasing the number of reflections used to form the lattice image will up to a limit increase the amount of structural information present in the

image. A restriction is imposed on this as the resolution of the microscope is limited. Inclusion of diffracted beams from planes of atoms of spacing smaller than the resolution capabilities of the microscope will only contribute additional noise to the image and so reduce image contrast. In addition, phase changes caused by spherical aberrations in the objective lens will tend to modify image contrast as more beams further from the optic axis are included. This effect will then hinder the direct interpretation of the image contrast on an intuitive basis. In general, the aperture should be just large enough to include beams from the fundamental lattice planes if an image representative of the crystal is to be obtained, e.g., the close packed planes in close packed structures.

The objective aperture is then positioned in the back focal plane so that it is exactly centered on the optic axis.

4. Adjustment of Illumination and Magnification (Imaging Mode). The condenser lenses and beam centering controls are set to produce a finely focused electron beam of maximum intensity, that is centered on the region of interest. The magnification is adjusted to a power suitable for observation of the fringe image (about 500,000x for 2Å fringes).

5. Focusing and Correction of Astigmatism. The area of interest is next focused. Preliminary corrections to astigmatism may be made using the Fresnel fringe at the edge of the foil, in a slightly over-focused condition. The fringe is adjusted, using the objective stigmator control, so that it appears even along a curved edge of the foil or around a hole in the foil. Final corrections to astigmatism are best

made in a focused condition, on the appearance of the background contrast. this should be adjusted so that there is no apparent directionality, using the objective stigmators.

6. Final Focusing, Through Focal Series and Recording the Image. The area of interest is brought into exact focus by either observing the disappearance of the Fresual fringe or using the focal position of minimum contrast of the background in the image. Optimum contrast in the image is not obtained at exact focus, a defocus of about -900Å is necessary to achieve suitable imaging conditions at 100 kV.[38] This is best obtained by recording a series of images at the finest intervals of focus. The series starting at exact focus and going to a defocus of about 1000Å. In recording the image exposure times should be kept as short as possible (not more than 15 sec) and the plates processed for maximum contrast.

The Interpretation of Lattice Fringe Images

Theory has established the validity of a number of approximations that, for strictly limited conditions may be made in the calculation of lattice images. These enable a direct intuitive interpretation of lattice images to be made as a projection of the potential in the specimen, provided the necessary experimental limitations are observed.[20] These limitations have been comprehensively reviewed[37,38] and are summerized here:

1. The spacing of contrast features in the image i.e., atoms or atom concentrations, must be within the resolution limits of the microscope (3.5Å typical at 100 kV).

2. The crystal should be no thicker than 150Å.

3. The crystal should be oriented with a principal axis of the lattice no more than 3×10^{-3} radians from the direction of the incident beam (symmetrical zone axis orientation).

4. Astigmatism and focusing of the objective lens must be optimum. A typical defocus of 400Å is indicated by calculations for 100kV electrons and a spherical observation coefficient of 1.8 mm for the objective lens.[38] Sufficient beams, to produce a representative image, must be used. The number depends on the structure, e.g., representative images have been produced using as few as five diffracted beams in germanium[21] whereas, as many as 100 beams are required in more complex structures.[37]

The procedures outlined above and presented in schematic form in Fig. 34 provide a means by which these conditions may be realized. Satisfaction of all these conditions is not always practical. However, several computer programs are available which enable the effects of lens abrevations, foil thickness and diffracting conditions on the image, to be calculated. Comparison of experimental images with images calculated from a postulate structure for several different optical conditions then enables structure analysis and refinment to be performed.

Useful information on phase transformations[41] stacking periodicities[32] and crystal defects[42] may be obtained using the less exacting technique of fringe imaging. Here single or a systematic row of diffracted beams are used to form a one dimensional fringe image which is representative of periodicities in a single crystallographic direction. Again the selection of the thinnest regions of the specimen, the use of precise diffracting conditions and attainment of optimum conditions of objective

lens stigmation and focusing are desirable but are not essential for a meaningful interpretation of the fringe image.

Optical Diffraction from Lattice Fringes

In addition to providing direct structural information about crystals, lattice imaging with laser diffraction provides a useful technique for obtaining selected area diffraction information from very small areas of the specimen. In selected area electron diffraction techniques such information is limited to regions not less than 1μ across (100 kV) by spherical aberrations in the objective lens.

By using the periodic variations in emulsion density of a lattice image recorded on film, as a diffraction grating for a laser light source, the optical diffraction pattern of the fringe image can be obtained.[43] As the fringes have a direct correspondence to periodicities within the crystal the optical diffraction pattern will contain the same geometrical information as the reflections in the electron diffraction pattern used to form the image. The technique is not limited by spherical aberrations so diffraction information and lattice from regions as small as 10Å across.[39,40] Since optical diffraction relies only on the periodic fluctuations of contrast in recorded image it may be used to determine the spacings in any periodic feature in the image, e.g., regular arrangements of stacking faults dislocations or precipitates.

REFERENCES

1. K. H. Jack and W. I. Wilson, 1972, Nature Phys Sci. (London), vol. 238, p. 28.

2. Y. Oyama and O. Kamigaito, 1972 Japan J. Appl. Phys., vol. 10, p. 1637.

3. A. Tsuge, H. Inoue and K. Komeya, 1972, Tenth Symposium on Basic Ceramics, Osaka.

4. K. Jack, 1976, J. Mat. Sci., vol. 11, p. 1135.

5. D. P. Thompson, 1976, J. Mat. Sci., vol. 11, 1377.

6. I. C. Huseby, H. L. Lukas and G. Petzow, 1975, J. Amer. Ceram. Soc., vol. 58, p. 377.

7. L. J. Gauchler, H. L. Lukas and G. Petzow, 1975, J. Amer. Ceram. Soc., vol. 58, p. 346.

8. P. J. Lumby, B. North and A. J. Taylor, "Special Ceramics 6," 1975, Stoke-on-Trent B. Ceram. R. A., p. 283.

9. R. R. Wills, R. W. Stewart and J. M Wimmer, 1976, Amer. Ceram. Soc. Bull., vol. 55, p. 975.

10. C. A. Andersson, F. F. Lange and J. L. Iskoe, 1975, Westinghouse electric corporation technical report, 3 October 15.

11. G. R. Terwilliger and F. F. Lange, 1975, J. Mat. Sci., vol. 10, p. 1169.

12. R. R. Wills, R. W. Stewart, J. A. Cunningham and J. M. Wimmer, 1976, J. Mat. Sci., vol. 11, p. 749.

13. P. Drew and M. H. Lewis, 1974, J. Mat. Sci., vol. 9, p. 1833.

14. L. S. Ransdell, 1947, Amer. Min., vol. 32, p. 64.

15. R. Paulus, 1933, Z. Physikal. Chem., vol. 22B, p. 305.

16. P. Eckerlin and A. Rabenou, 1960, Z. Anovg, Ally. Chem., vol. 304, p. 218.

17. L. Hall, G. E. Guvr and G. A. Jeffrey, 1969, Z. Anovg, Allg. Chem., vol. 369, p. 108.

18. P. Echerlin, 1967, Z. Anovg. Ally. Chem., vol. 353, p. 225.

19. W. L. Bell, 1976, J. Appl. Phys., vol. 47, p. 1676.

20. M. A. O'Keefe, 1973, Acta. Cryst., vol. A29, p. 389.

21. J. Desseaux, A. Kenault and A. Bourvet, 1977, Phil. Mag., vol. 35, p. 357.

22. S. Iijima and P R. Buseck, in Electron Microscopy in Mineralogy, H. R. Wenk, ed., p. 319.

23. S. Andersson and B. G. Hyde, 1974, J. Solid State Chem., vol. 9, pp. 92-101.

24. C. M. Drum, 1965, Phil. Mag., vol. 11, p. 313.

25. R. Gevers, A. Art and S. Amelinckx, 1963, Phys. Sat. Sol., vol. 3, p. 1563.

26. P. B. Hirsch, et al., Electron Microscopy of Thin Crystals (Butterworths, London, 1965), p. 165.

27. R. Serneels, M. Snykers, P. Delavignette, R. Gevers and S. Amelinckx, 1973, Phys. Sat. Sol., Vol. B58, p. 277.
O. Van der Biest and G. Thomas, 1975, Acta. Cryst. vol A31, p. 70.

28. J. V. Landuyt, 1974, J. de Physique, vol. 35, p. C7-53.

29. S. Iijima and J. G. Allpress, 1973, J. Solid State Chem., vol. 7, p. 94.

30. S. Iijima, 1975, Acta. Cryst., vol. A31, p. 784.

31. K. H. Jack, private communication.

32. J. D. McConnell, J. L. Bucthison and J. S. Anderson, 1974, Proc. R. Soc. London, vol. A339, p. 1.

33. J. Van Landuyt, S. Amelinckx, J. A. Kolm and D. W. Eckart, 1974, J. Solid State Chem., vol. 9, p. 103.

34. P. R. Okamoto and G. Thomas, Acta. Met., 1971, vol. 19, p. 825.

35. D. F. Lynch, A. F. Moodie and M. A. O'Keefe, Acta Cryst., 1973, vol. A31, p. 300.

36. B. V. Johansen, Micron, 1973, vol. 4, p. 121.

37. J. G. Allpress and S. V. Sanders, J. Appl. Cryst., 1973, vol. 6, p. 165.

38. J. M. Cowley and S. Iijima in Electron Microscopy in Mineralogy, H. R. Wenk, ed., Springer-Verlag, 1976.

39. R. Sinclair, R. Gronsky and G. Thomas, Acta. Met., 1976, vol. 24, p. 789.

40. D. R. Clarke and G. Thomas, 34th Annual Proc. Electron Microscopy Soc. Amer., Miami Beach Flordia, 1976, W. Bailey, ed.

41. R. Sinclair, K. Schneider and G. Thomas, Acta Met. (1975), vol. 23, p. 873.

42. J. Van Landuyt and S. Amelinckx, Mat. Res. Bull (1971), vol. 6, p. 613.

43. S. G. Lipson and H. Lipson, Optical Physics, Cambridge University Press (1969).

Table I. Values of ' phase factor $\alpha = 2\pi\, g \cdot R$ for various g and R for faults in $BeSiN_2$ structure.

R	P	1/2 C	P + 1/2 C	P - 1/2 C
$2\pi\, g$	1/3[100]	1/2[001]	1/6[203]	1/6[203]
$2\pi(\bar{0}02)$	0	0	0	0
$2\pi(\bar{2}0\bar{1})$	$+2/3\pi$	π	$-1/3\pi$	$-1/3\pi$
$2\pi(\bar{2}00)$	$+2/3\pi$	0	$+2/3\pi$	$+2/3\pi$
$2\pi(\bar{4}00)$	$-2/3\pi$	0	$-2/3\pi$	$-2/3\pi$
$2\pi(\bar{6}00)$	0	0	0	0
$2\pi(320)$	0	0	0	0

Table II. Compositions and C spacings of polytypes in the $BeSiN_2$-Be_3N_2 series.

Polytype	M:X	# Layers Be_3N_2	# Layers $BeSiN_2$	Compositions		C Spacings Å	
				Predicted	Experimental*	Predicted	Experimental*
4H/Be_3N_2	3:2	4	--	Be_3N_2	Be_3N_2	9.693	9.693
9R	4:3	6	3	Be_7SiN_6	--	12.567	--
8H	5:4	4	4	Be_4SiN_4	Be_4SiN_4	19.064	19.22
15R	6:5	6	9	$Be_9Si_3N_{10}$	$Be_9Si_3N_{10}$	35.625	36.32
12H	7:6	4	8	$Be_5Si_2N_6$	$Be_5Si_2N_6$	28:44	29.10
21R	8:7	6	15	$Be_{11}Si_5N_{14}$	$Be_{11}Si_5N_{14}$	49:68	50.98
16H?	9:8	4	12	$Be_6Si_3N_8$	--	37.81	--
27R?	10:4	6	21	$Be_{13}Si_7N_{18}$	$Be_{13}Si_7N_{18}$	63.74	65.11
$BeSiN_2$	1:1	-	2	$BeSiN_2$	$BeSiN_2$	4.69	4.69

Close packed layer spacing β Be_3N_2 = 2.423Å.
Close packed layer spacing $BeSiN_2$ = 2.343Å.

*From Huesby, et al.[6]

Table III. Compositions and C spacings of polytypes in the BeO-Be_3N_2 series.

Polytype	M:X	# Layers Be_3N_2	# Layers Be_2O_2	Compositions		C Spacings Å	
				Predicted	Experimental*	Predicted	Experimental*
4H/Be_3N_2	3:2	4	—	Be_3N_2	Be_3N_2	9.693	9.693
9R	4:3	6	3	Be_4ON_2	--	21.099	--
8H	5:4	4	4	$Be_5O_2N_2$	--	18.44	--
15R	6:5	6	9	$Be_6O_3N_2$	$Be_6O_3N_2$	34.22	34.58
12H	7:6	4	8	$Be_7O_4N_2$	--	17.19	
21R	8:7	6	15	$Be_8O_5N_2$	$Be_8O_5N_2$	47.34	47.87
16H?	9:8	4	12	$Be_9O_6N_2$	--	35.94	--
27R?	10:9	6	21	$Be_{10}O_7N_2$	--	60.47	61.05
BeO	1:1	-	2	BeO	BeO	4.38	4.38

Close packed layer spacing of β Be_3N_2 = 2.423Å.
Close packed layer spacing of BeO = 2.187Å.

*From Huesby, et al.[6]

FIGURE CAPTIONS

Fig. 1. The Si_3N_4-Be_3N_2-BeO-SiO_2 (1800°C) system represented using equivalent concentrations (D. P. Thompson[5]).

Fig. 2. Low magnification electron micrograph of Be_3N_2 grains, sample 1. Note dense impurity phase at grain boundaries and triple points.

Fig. 3. Electron diffraction patterns from single grains of Be_3N_2 (a) (111) pole of α form, (b) (110) pole of α form, (c) (001) pole of α form, (d) (01.0) pole of β form, and (e) (00.1) pole of β form.

Fig. 4. Ordered domains of $BeSiN_2$ structure (001) orientation (a) bright field, (b) dark field taken using two superlattice reflections arrowed in (c). (c) SAD from regions containing large domains of the three ordered varients of $BeSiN_2$ and (d) SAD showing diffuse superlattice reflections from an adjacent region.

Fig. 5. 2-1/2 D image pair of ordered varients in $BeSiN_2$ taken using reflections in Fig. 4(c). (a) 1000Å underfocused, (b) 1000Å overfocused.

Fig. 6. SAD from a well ordered region of 15R polytype structure, (010) orientation. The reflections arrowed are those used in the formation of the image in Fig. 11.

Fig. 7. Direct resolution of the block spacing 12.1Å of a 15R polytype.

Fig. 8. Direct lattice fringe image in which the individual close packed planes (2.4Å) can be seen. In this relatively perfect region each block consists of five close packed planes.

Fig. 9. Low magnification electron micrograph of a typical region of sample 2 showing the banded appearance of the grains.

Fig. 10. An adjacent region to that of Fig. 8. Departures from the ideal polytype arrangement are seen directly with blocks comprising of only four close-packed planes and others six.

Fig. 11. Two dimentional structure image of a region of predominantly 15R polytype structure in which the close packed planes 2.4Å and crossfringes can be directly seen. The corresponding diffraction pattern, (010) orientation, is inset.

Fig. 12. Comparison of an enlarged region of Fig. 11 with the projected 15R structure in the same orientation. The black triangles represent rows of nitrogen tetrahedra occupied by beryllium and silicon atoms, the shaded triangles rows of nitrogen tetrahedra occupied by beryllium atoms alone. The white triangles correspond to tunnels of vacant nitrogen tetrahedra in the structure. Marked are the outlines of three identical structural blocks which make up the unit cell.

Fig. 13. The effect of tilting on contact across a twin boundary in a disordered 15R polytype structure. (a) Bright field in a symmetrical (010) orientation, (b) and (c) bright field images of the boundary, when tilted a small amount about the directions indicated by the arrows. Differential contrast

is seen between the twins. SAD from either side and across the boundary confirms the twin relation.

Fig. 14. Comparison of a high resolution image of block spacings in a polytype structure which the image of twin bands in the same region made visible by tilting. Associated with each twin boundary is a disordered block spacing.

Fig. 15. Direct resolution of the block spacings across a single grain of polytype structure showing an intergrowth between a well ordered 15R structure (top left) and a well ordered 8H structure (bottom left) via a disordred region.

Fig. 16. (a-c) SAD patterns from regions of 15R, disordered and 8H polytype structures in Fig. 15. (d-h) Optical diffraction patterns from Fig. 15 (see text).

Fig. 17. Twin terminations in a polytype grain made visible by tilting away from an (010) orientation.

Fig. 18. Contrast behavior of a twin termination under diffracting conditions (a) (100) symmetrical orientation, (b) g = 040, (c) 00ℓ systematic row of reflections excited, (d) SAD symmetrical (100) pole.

Fig. 19. Schematic diagram of the twin termination in Fig. 18. The [100] foil normal is marked.

Fig. 20. Complicated fault fringe contrast arising from overlapping disorders in stacking in the close-packed planes of the 15R polytype structure. Several stacking faults are seen to terminate within the grain at a dislocation.

Fig. 21. Dislocations in the close packed planes of a polytype grain (001) orientation (a) $g = 040$, (b) $g = 320$, (c) $g = 3\bar{2}0$ SAD pattern from this region (d) indicates the grain has a disordered polytype structure.

Fig. 22. The (010) projection of a terminating twin three blocks wide. the disorders accommodating the twin at the coherent twin boundaries are seen to displace the position of the M_2X layer in the twin one close packed layer spacing relative to the matrix.

Fig. 23. Atom position and displacements necessary to accommodate the twin termination in the region outlined in Fig. 22.

Fig. 24. Diagram of block displacements in the matrix necessary to accommodate a terminating twin in a rhombohedral polytype structure. The new position of the M_2X layer in the twin is indicated by the dotted lines.

Fig. 25. Contrast from isolated faults in a $BeSiN_2$ grain for the diffracting conditions (a) $g = 002$, (b) $g = \bar{2}0\bar{1}$, (c) $g = \bar{2}00$, (d) $g = \bar{4}00$, (e) $g = \bar{6}00$ and (f) $g = 320$.

Fig. 26. Bright field and two dark fields of enantiomorphic domains in $BeSiN_2$. Differential contrast between domains arises in dark field (b) $g = 002$ and (c) $g = 00\bar{2}$. The corresponding diffracting condition is shown in (d). Operating voltage is 650 kV.

Fig. 27. Bright field image of faults in a grain of $BeSiN_2$ structure (010) orientation. Faults in the close packed planes are reviewed edge on. Note the strain contrast associated with the faults and the occurrence of fault pairs.

Fig. 28. High density of faults in the close-packed planes of a single grain of sample 4 (a) bright field image, to the right the grain remains fault free. (b) Dark field image of the faults taken using the streak produced by the faults (see inset SAD).

Fig. 29. Fig. 29. A series of bright field images taken across a single grain of highly faulted $BeSiN_2$ structure.

Fig. 30. Electron and optical diffraction patterns taken from Fig. 29 (see text).

Fig. 31. Diagram of the stacking produced by a single fault in the close packed plane of a wurtzite structure $R = 1/6(203)$ (referred to $BeSiN_2$ unit cell). (010) orientation planar section. (a) Unfaulted structure, (b) faulted structure.

Fig. 32. Diagram showing the formation of fringe images from a periodic structure.

Fig. 33. Schematic of diffraction pattern/objective aperture configurations for (a) Axial illumination, (b) tilted beam, systematic now, (c) tilted beam symmetrical diffraction pattern. The open circle denotes the transmitted beam; the optic axis is located at X.

Fig. 34. Schematic of lattice imaging procedures.

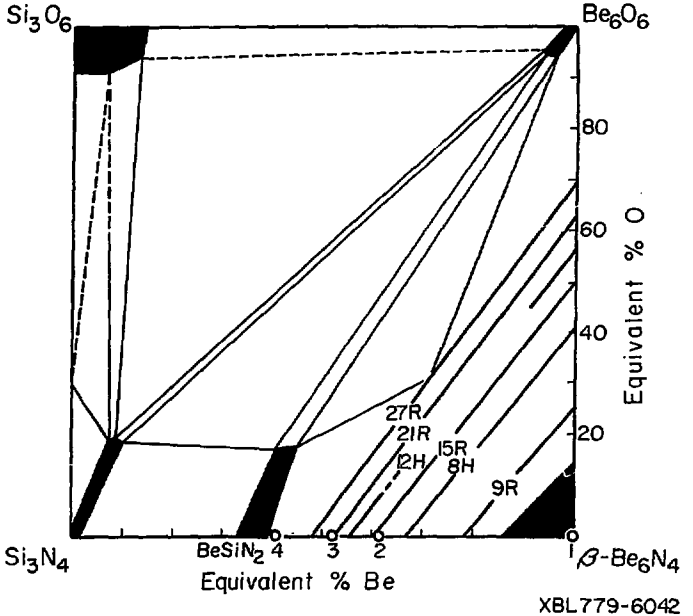
Si_3O_6
Be_6O_6
80
60
40
20
Equivalent % O
27R
21R
15R
12H
8H
9R
Si_3N_4
$BeSiN_2$
4
3
2
1
β-Be_6N_4
Equivalent % Be
XBL779-6042

Fig. 1

XBB 779-8401

Fig. 2

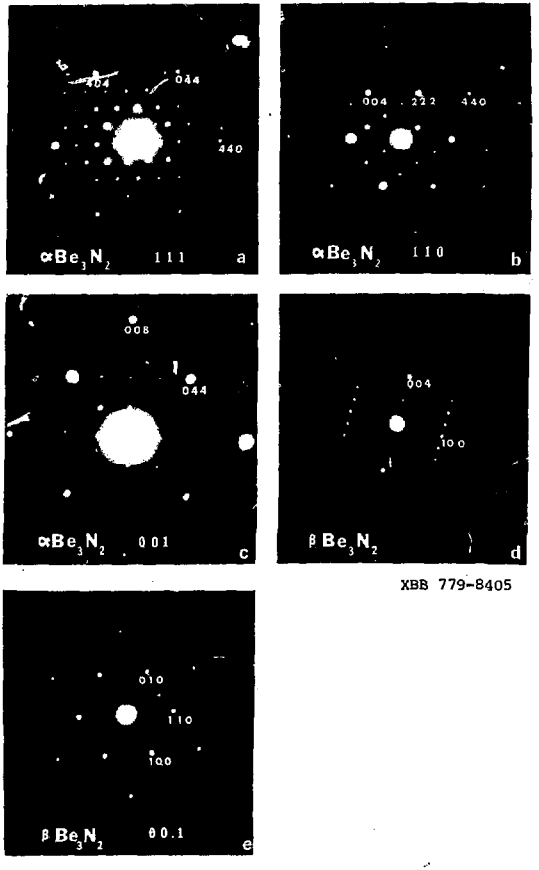

XBB 779-8405

Fig. 3

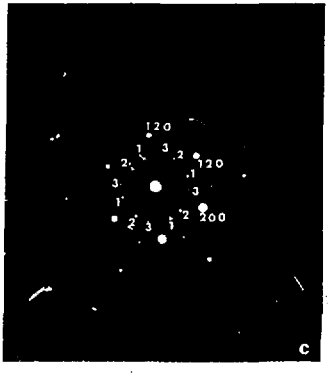

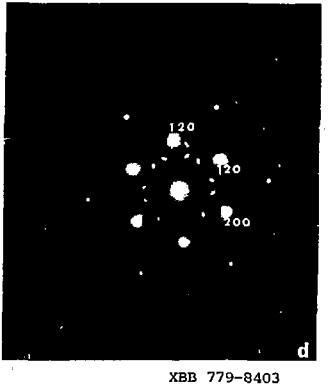

XBB 779-8403

Fig. 4

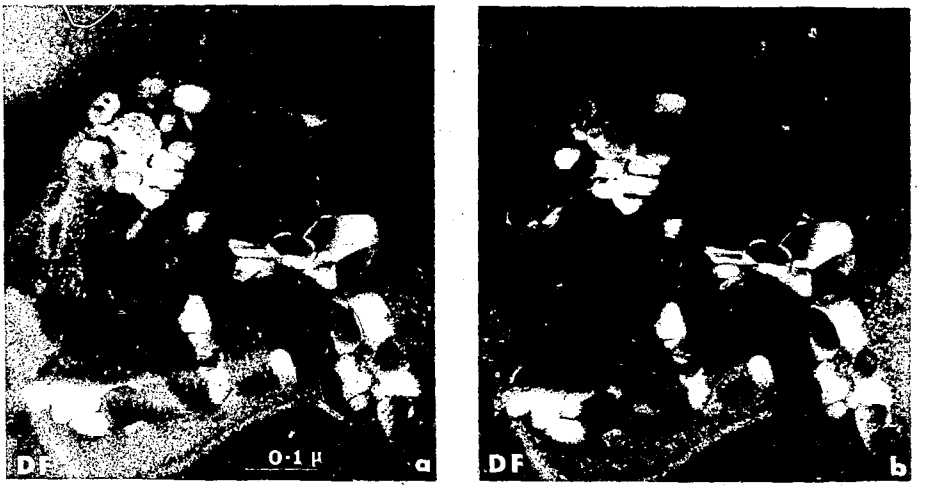

XBB 779-8407

Fig. 5

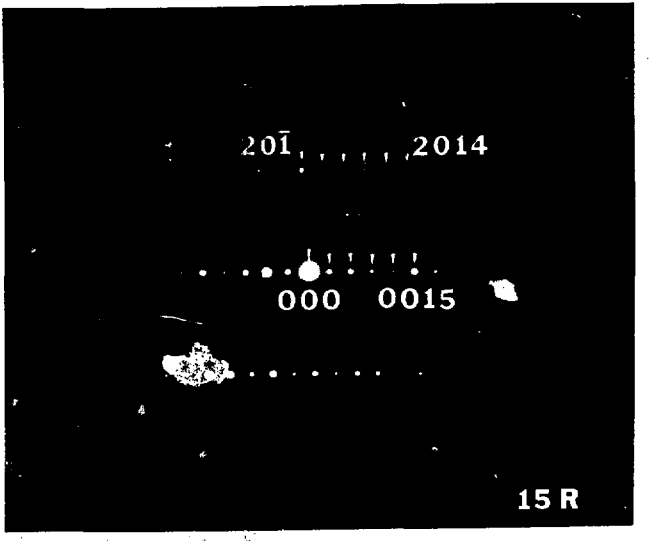

XBB 779-9255

Fig. 6

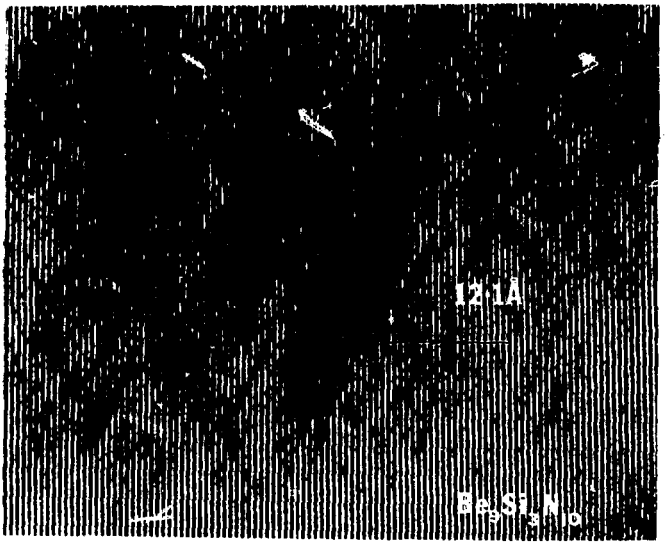

XBB 771-592

Fig. 7

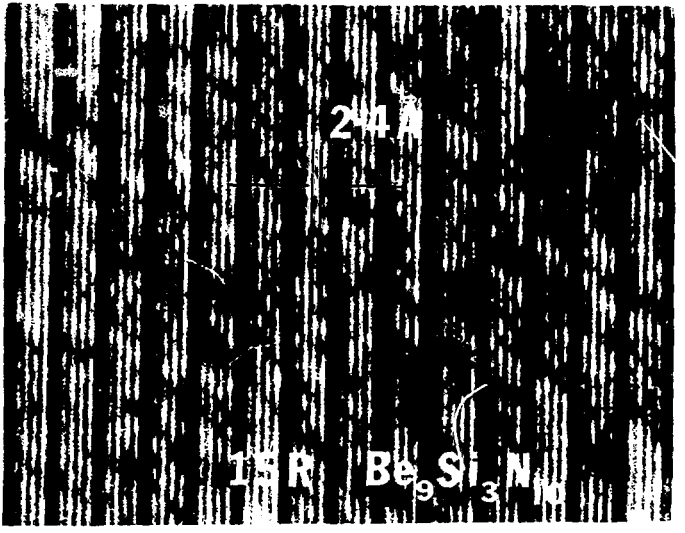

XBB 771-596

Fig. 8

XBB 772-892

Fig. 9

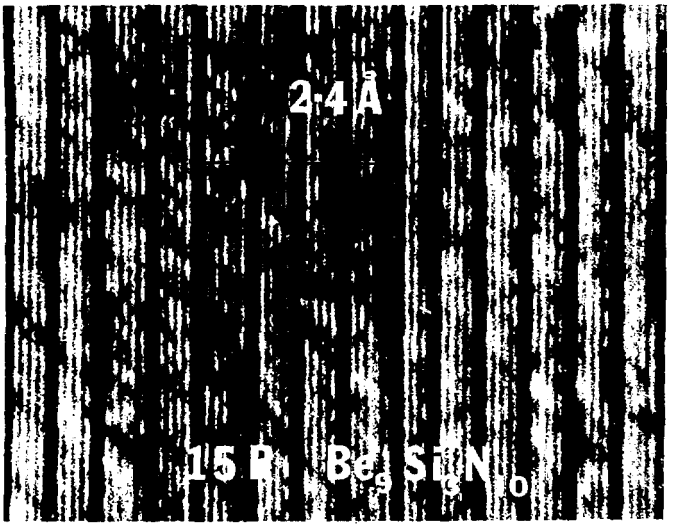

XBB 771-597

Fig. 10

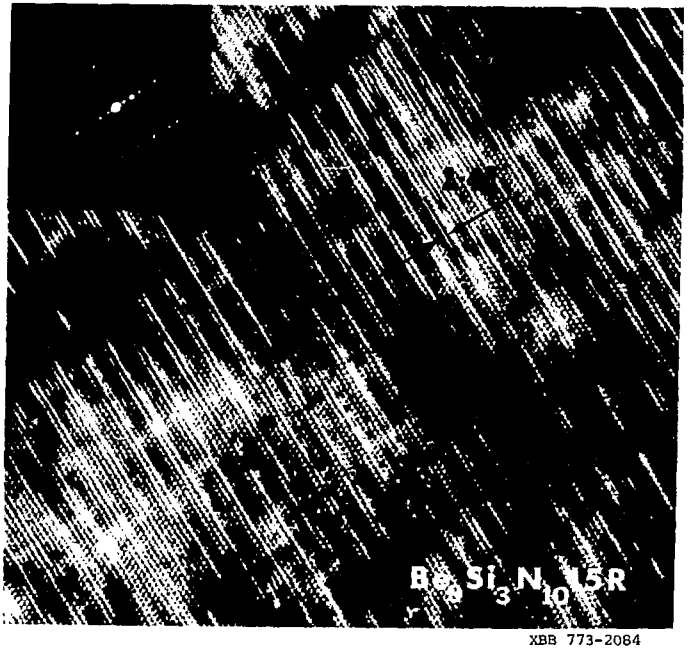

XBB 773-2084

Fig. 11

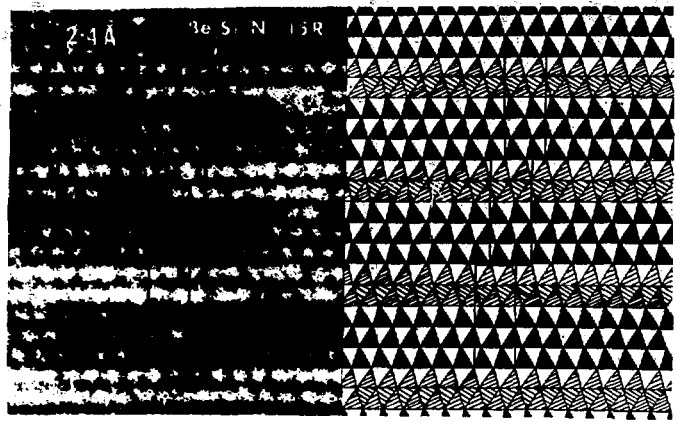

XBB 775-4855

Fig. 12

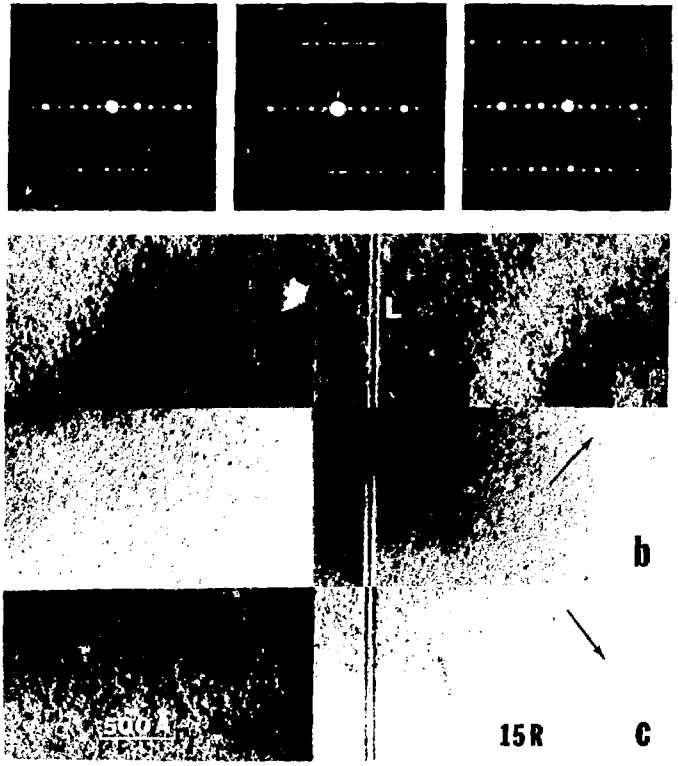

XBB 775-4851

Fig. 13

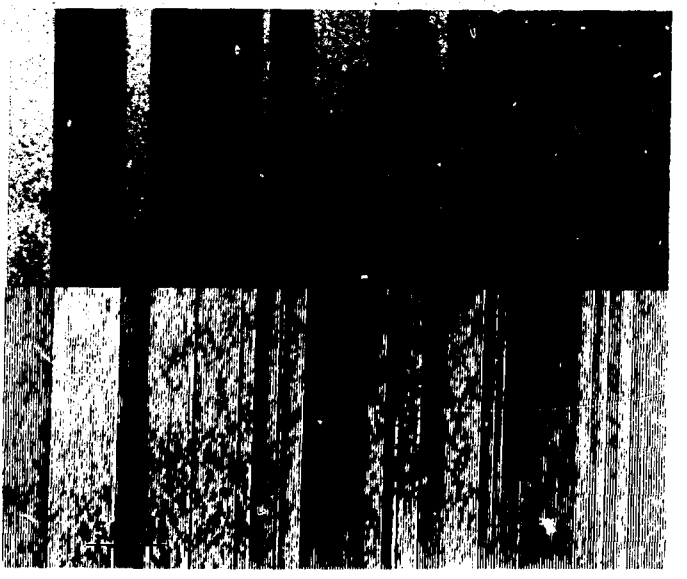

XBB 775-4854

Fig. 14

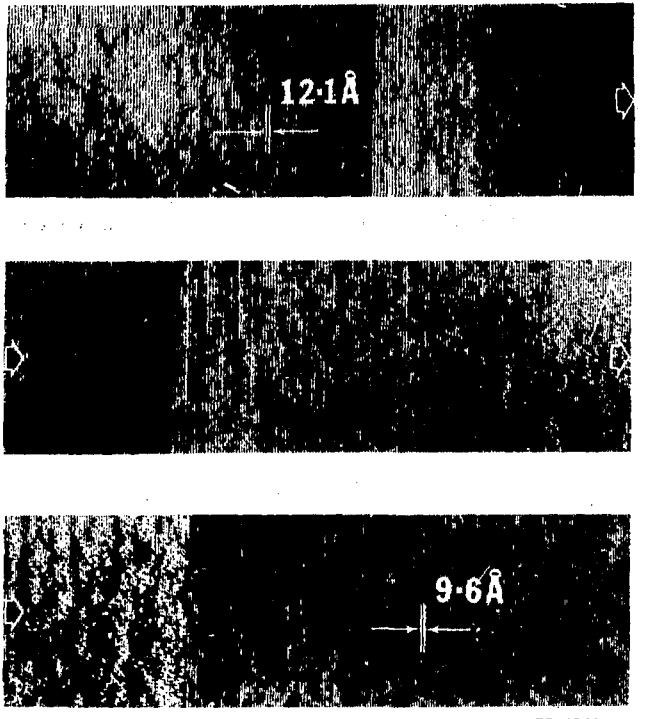

XBB 775-4852

Fig. 15

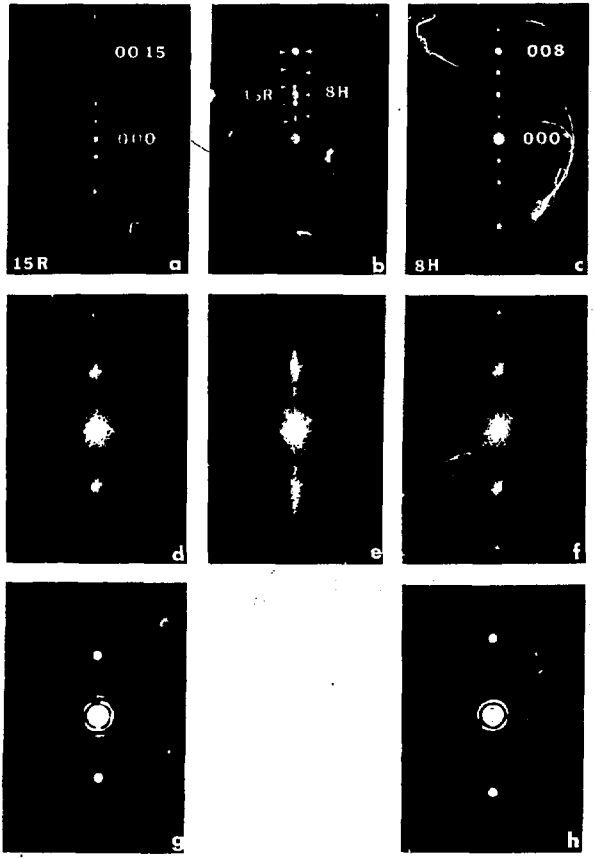

XBB 779-4810

Fig. 16

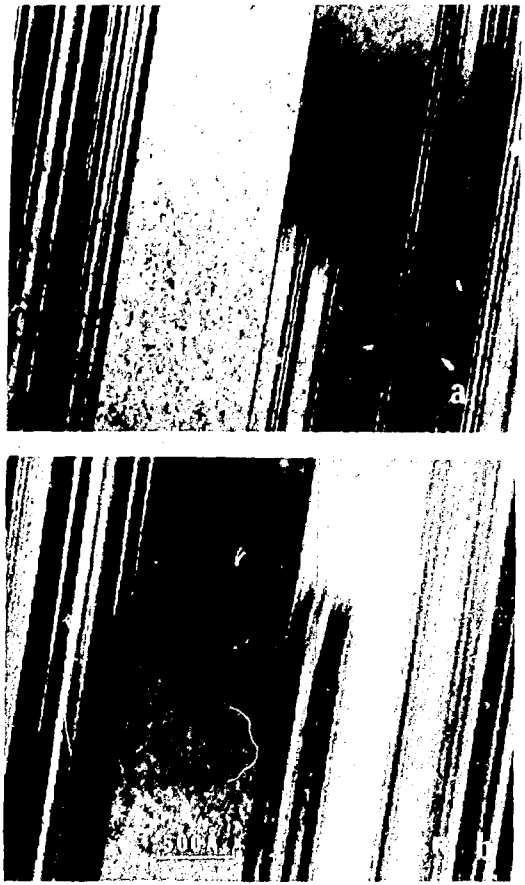

XBB 775-4853

Fig. 17

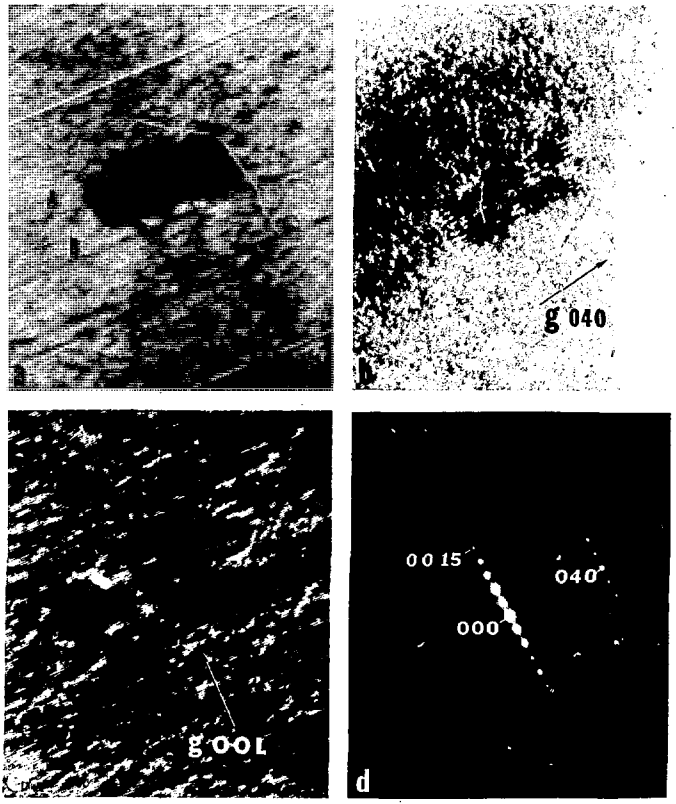

XBB 779-4806

Fig. 18

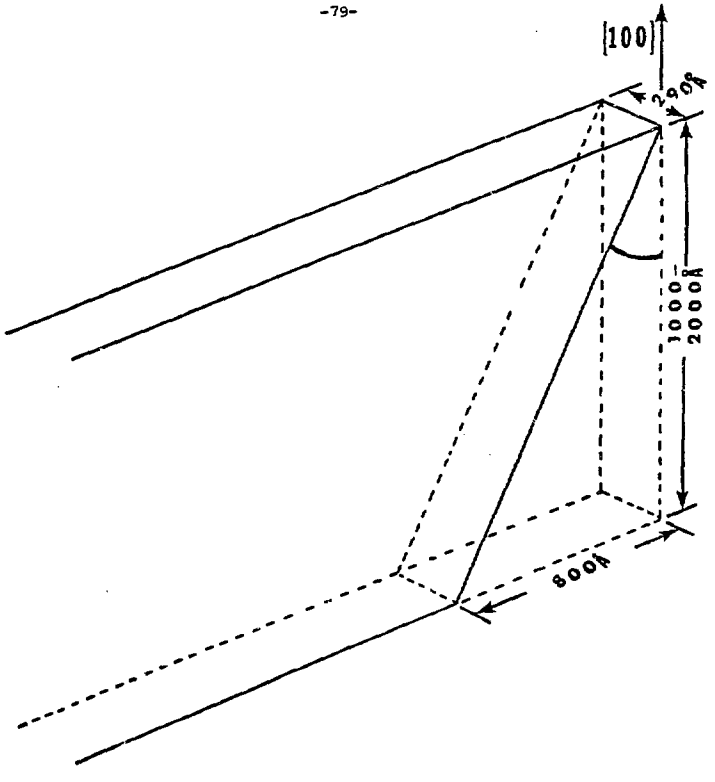

XBL 778-2865

Fig. 19

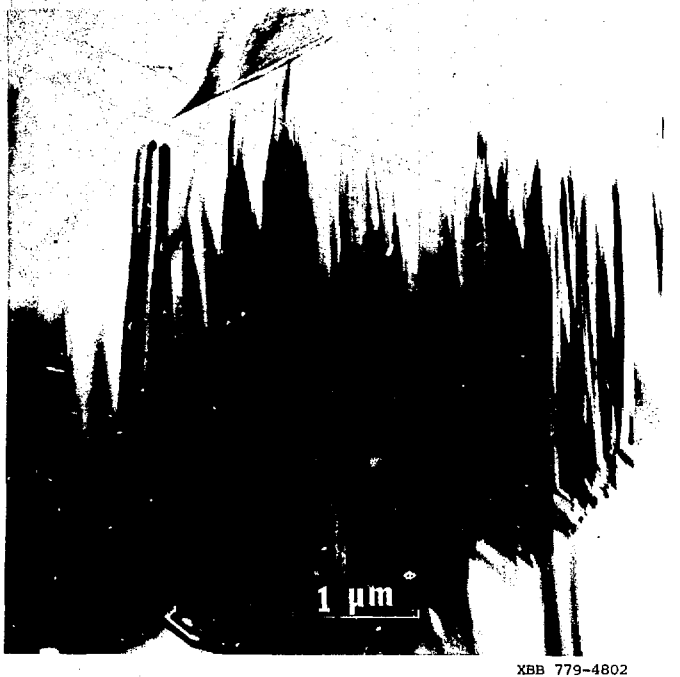

XBB 779-4802

Fig. 20

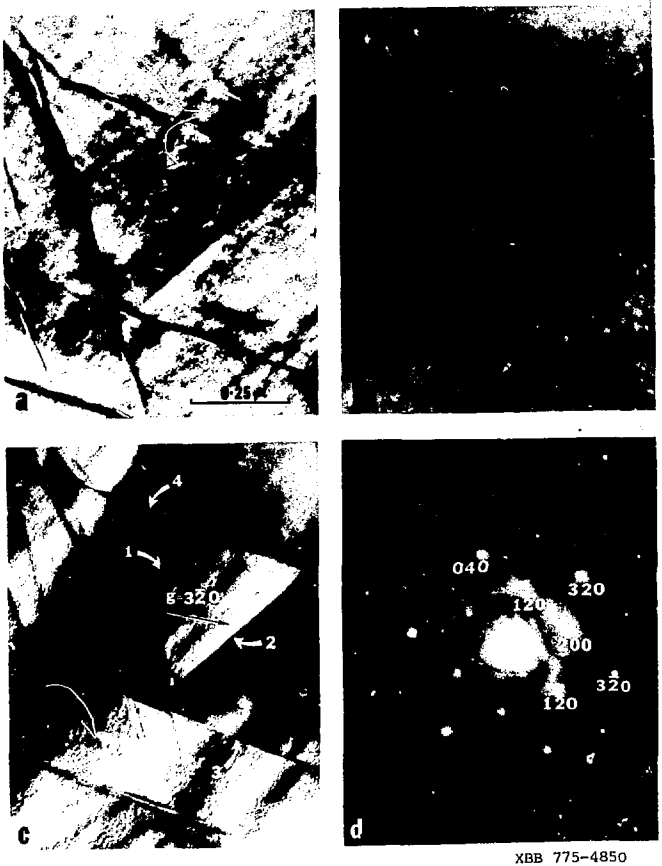

XBB 775-4850

Fig. 21

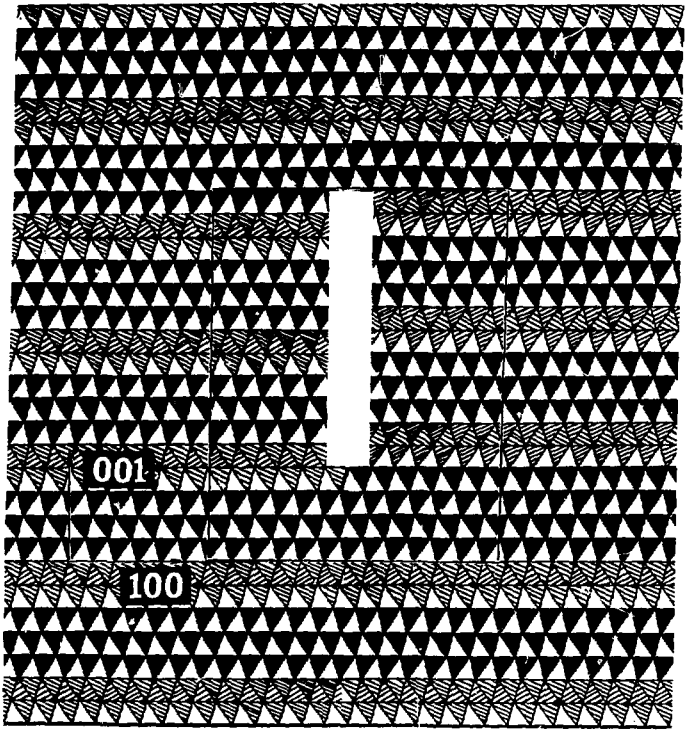

XBL 778-2866

Fig. 22

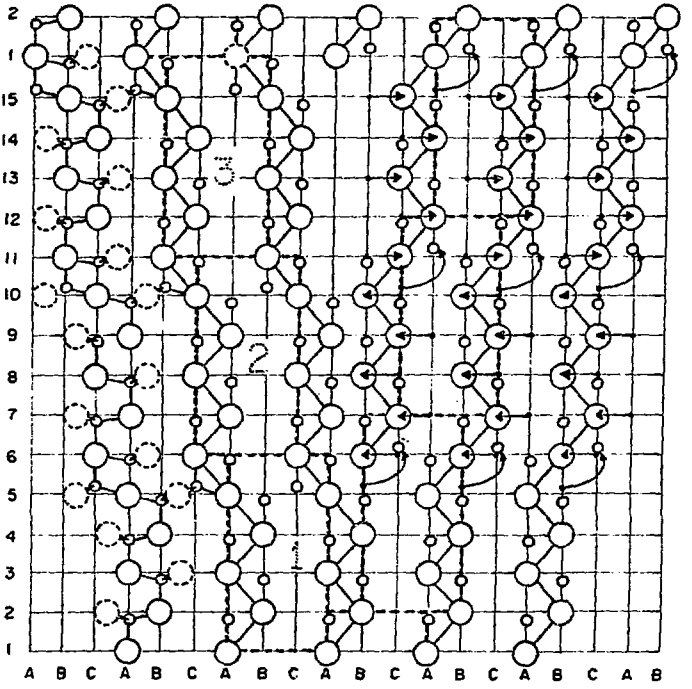
2
1
15
14
13
12
11
10
9
8
7
6
5
4
3
2
1
A B C A B C A B C A B C A B C A B C A B
o Metal atom sites Be, Si
Non metal atom sites, N
XBL779-6044

Fig. 23

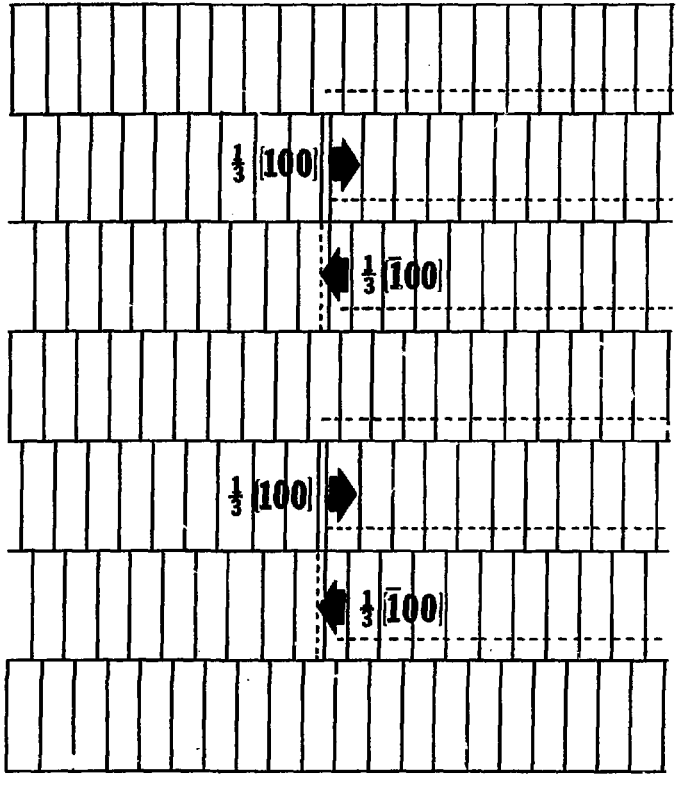

XBL 778-2864

Fig. 24

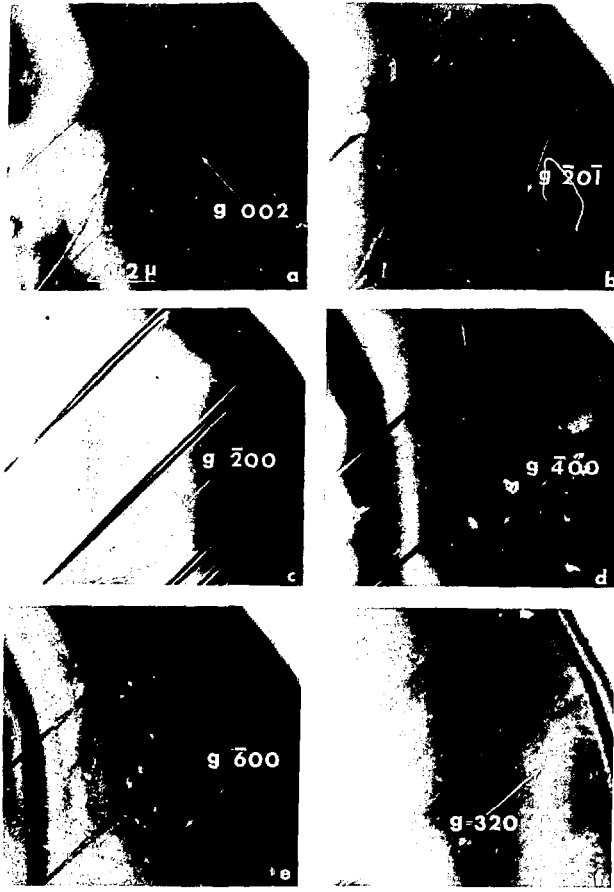

XBB 779-4812

Fig. 25

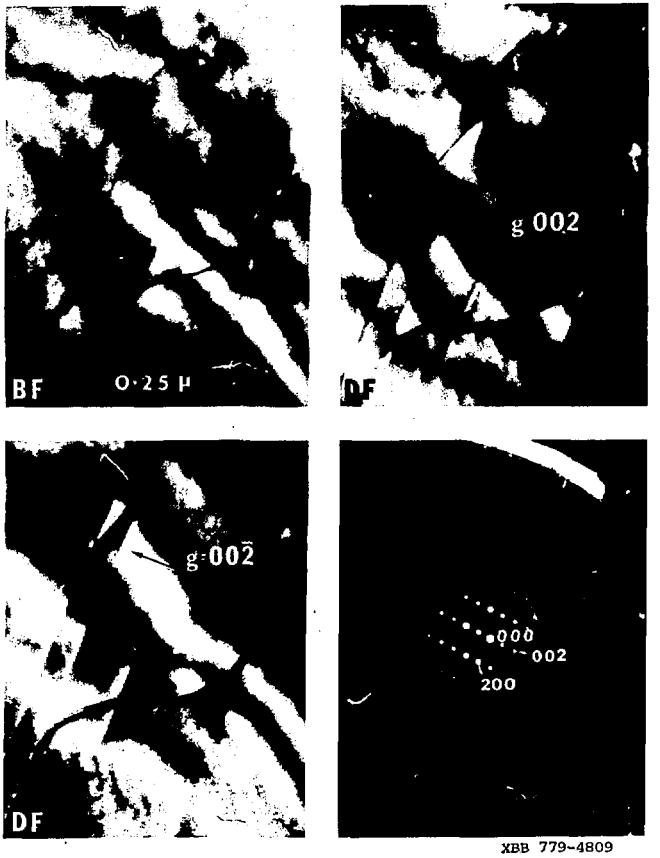

XBB 779-4809

Fig. 26

XBB 779-8404

Fig. 27

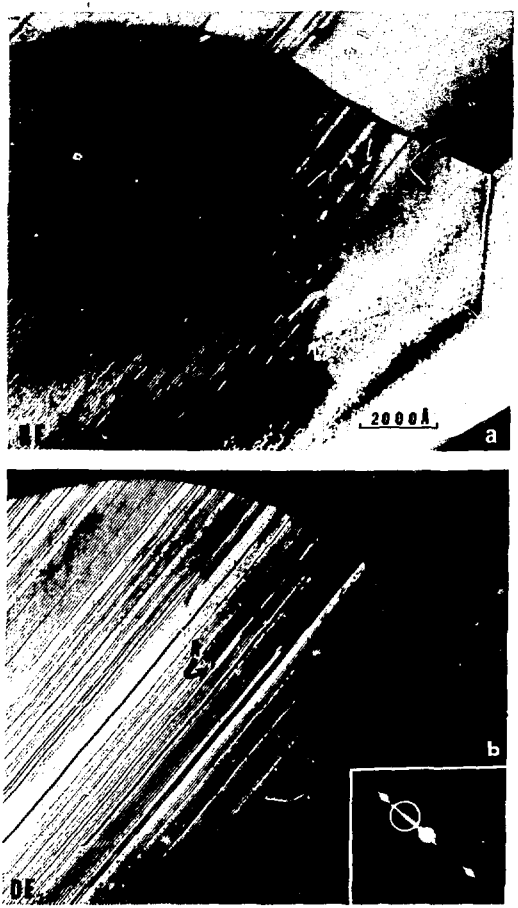

XBB 779-8411

Fig. 28

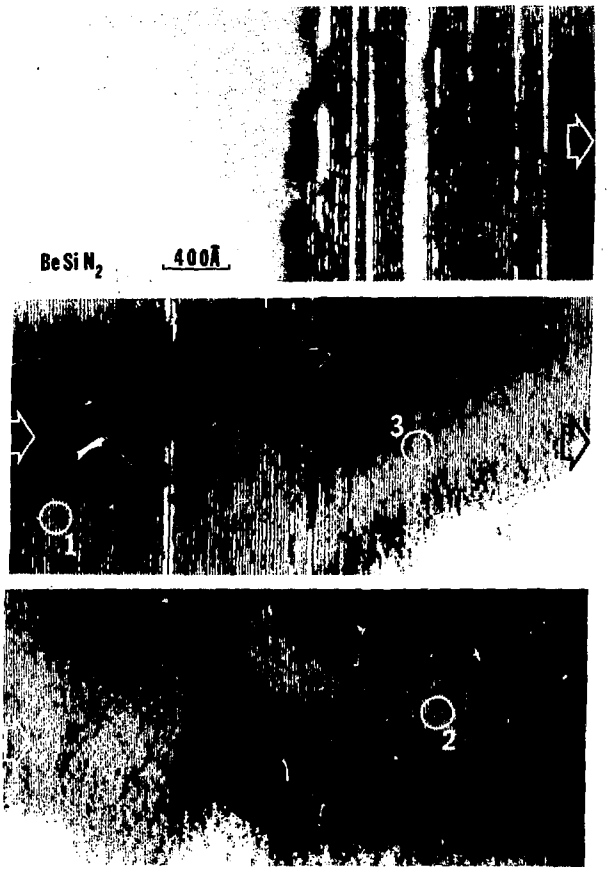

XBB 779-8408

Fig. 29

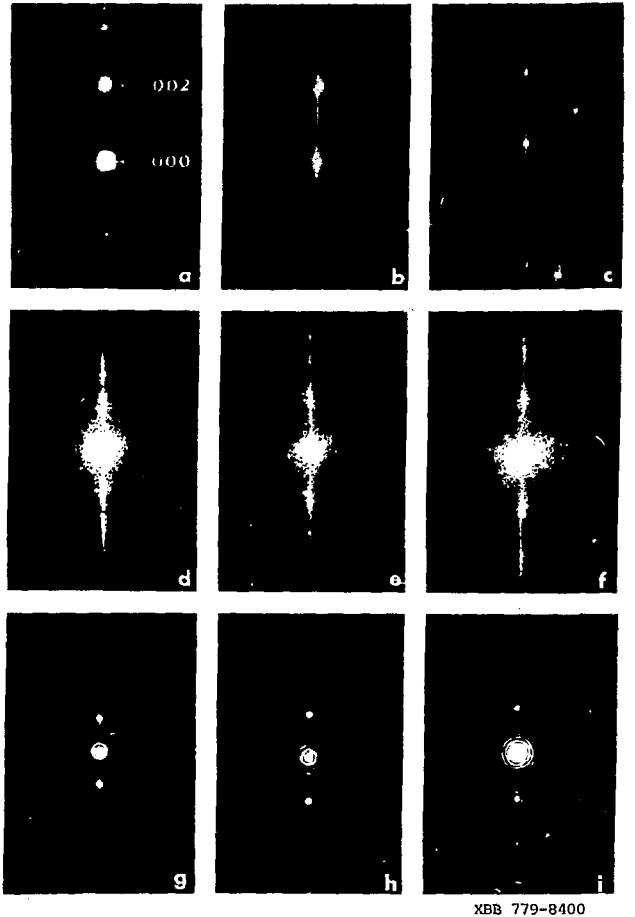

XBB 779-8400

Fig. 30

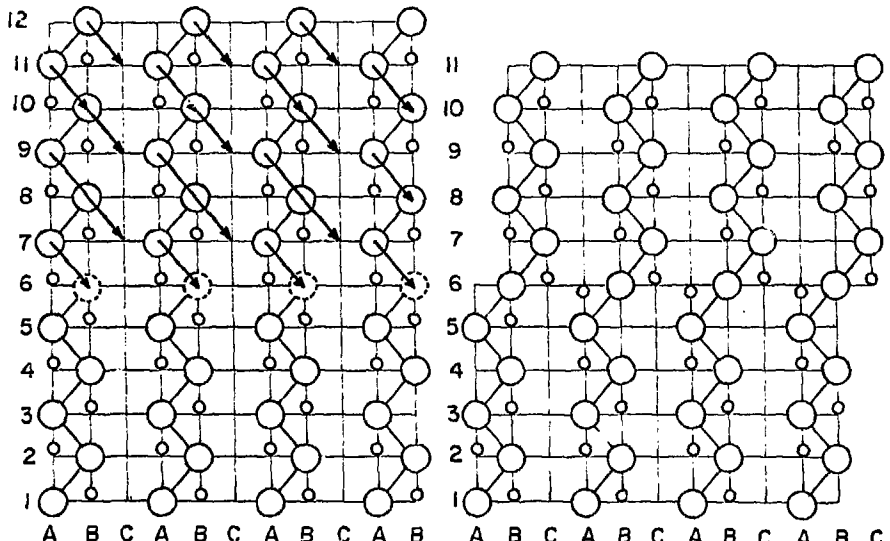

XBL 779-6043

Fig. 31

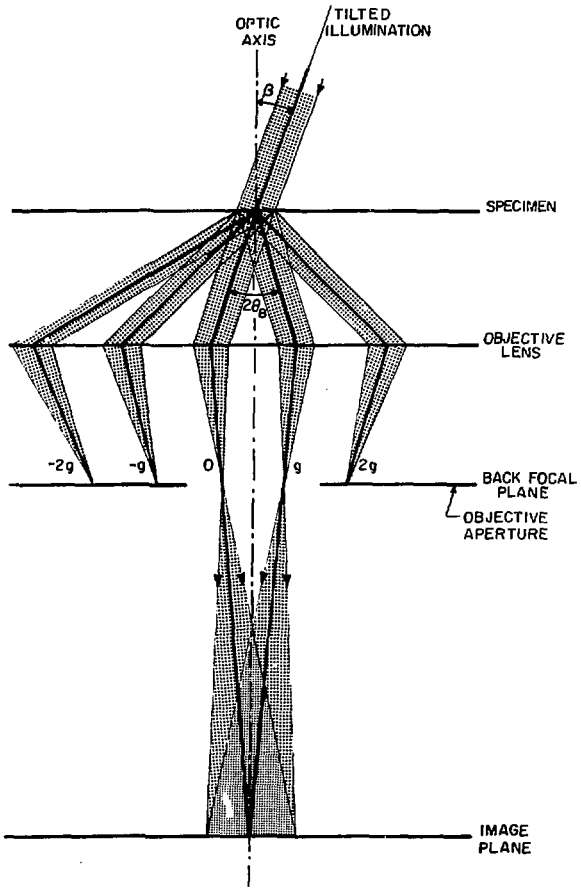
OPTIC AXIS
TILTED ILLUMINATION
β
SPECIMEN
2θB
OBJECTIVE LENS
-2g
-g
0
g
2g
BACK FOCAL PLANE
OBJECTIVE APERTURE
IMAGE PLANE
XBL 777-5749A

Fig. 32

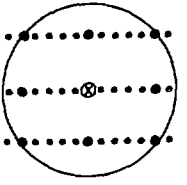

(a)

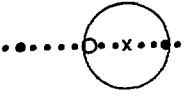

(b)

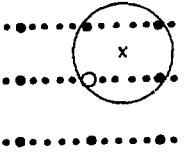

(c)

XBL 7710-6165

Fig. 33

LATTICE IMAGING

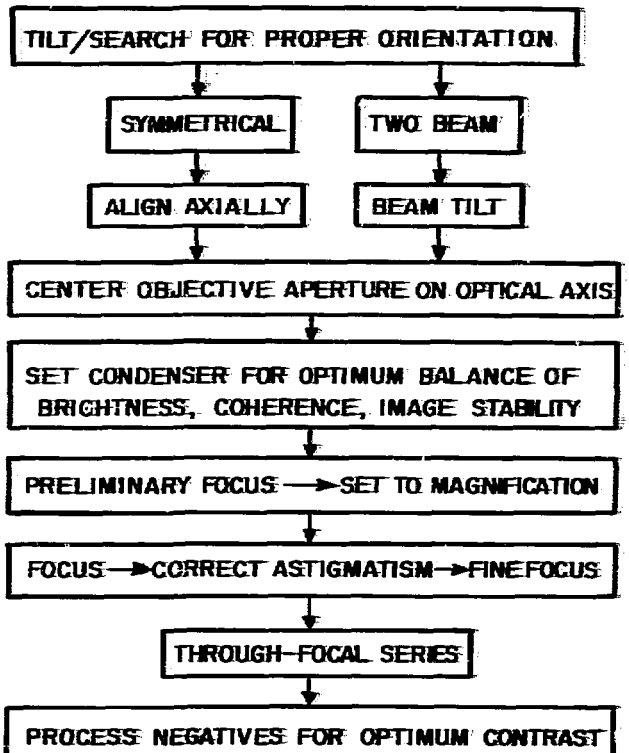

XBL768-7271

Fig. 34